

# Aligning Inductive Bias for Data-Efficient Generalization in State Space Models

Qiyu Chen<sup>1</sup> and Guozhang Chen<sup>2</sup>

<sup>1</sup>School of Physics, Peking University, China

<sup>2</sup>School of Computer Science, National Key Laboratory for Multimedia Information Processing, Peking University, China

<sup>1</sup>[cqy@stu.pku.edu.cn](mailto:cqy@stu.pku.edu.cn), <sup>2</sup>[guozhang.chen@pku.edu.cn](mailto:guozhang.chen@pku.edu.cn)

## Abstract

The remarkable success of large-scale models is fundamentally tied to scaling laws, yet the finite nature of high-quality data presents a looming challenge. One of the next frontiers in modeling is data efficiency: the ability to learn more from less. A model’s inductive bias is a critical lever for this, but foundational sequence models like State Space Models (SSMs) rely on a fixed bias. This fixed prior is sample-inefficient when a task’s underlying structure does not match. In this work, we introduce a principled framework to solve this problem. We first formalize the inductive bias of linear time-invariant SSMs through an SSM-induced kernel, mathematically and empirically proving its spectrum is directly governed by the model’s frequency response. Further, we propose a method of Task-Dependent Initialization (TDI): power spectrum matching, a fast and efficient method that aligns the model’s inductive bias with the task’s spectral characteristics before large-scale training. Our experiments on a diverse set of real-world benchmarks show that TDI significantly improves generalization and sample efficiency, particularly in low-data regimes. This work provides a theoretical and practical tool to create more data-efficient models, a crucial step towards sustainable scaling.

## 1 Introduction

The paradigm of scaling laws, wherein model performance predictably improves with more data, parameters, and compute, has driven unprecedented progress in AI [Kaplan et al., 2020, Hestness et al., 2017, Bahri et al., 2024]. However, this paradigm faces a critical bottleneck: the finite supply of high-quality training data [Shorten and Khoshgoftaar, 2019, Sun et al., 2017, Citovsky et al., 2021]. As we approach this data limit, the next wave of innovation must come from improving the data efficiency of our models [Shorten and Khoshgoftaar, 2019, Adadi, 2021]. A primary mechanism for achieving this is to improve models with an appropriate inductive bias. It is a set of built-in assumptions that guides the learning process towards plausible solutions, thereby reducing the reliance on massive datasets [Hastie et al., 2009, Battaglia et al., 2018, Goyal and Bengio, 2022].

State Space Models (SSMs) have emerged as a powerful and efficient architecture for sequence modeling [Gu et al., 2022a,b, Smith et al., 2023, Gu and Dao, 2023, Dao and Gu, 2024, Patro and Agneeswaran, 2025]. Foundational models like S4D are built on the linear time-invariant (LTI) principle, which forms the theoretical backbone of this entire model class. While recent advances such as Mamba [Gu and Dao, 2023, Dao and Gu, 2024] have introduced powerful input-dependent selective mechanisms, a formal understanding of their behavior must begin with the core LTI structure they are built upon. Foundational LTI-based models have a highly structured architecture that encodes inductive bias. Such bias becomes an efficiency bottleneck, requiring the model to first unlearn its preconceptions before learning the actual task [Gu et al., 2022b, Yu et al., 2024].

In this work, we directly address this source of inefficiency. We introduce a theoretical and practical framework to first understand and then dynamically align the inductive bias of LTI SSMs

with the task, improving generalization from smaller samples. Our contributions are summarized as follows:

1. **A Formal Theory of SSM Inductive Bias:** We establish a rigorous connection between LTI SSMs and kernel regression. We define a novel SSM-induced kernel and prove that its spectral decomposition, which governs learning dynamics and generalization, is determined by the SSM’s frequency response.
2. **A Practical, Data-Driven Initialization Method:** Building on this theory, we propose Task-Dependent Initialization (TDI), a method that uses power spectrum matching to efficiently shape the SSM’s initial parameters. This pre-aligns the model’s inductive bias with the task’s power spectrum, providing a customized and advantageous starting point for training. This is validated across a suite of real-world benchmarks.

## Related Work

Inductive bias shapes generalization by steering models toward solutions aligned with specific assumptions [Hastie et al., 2009]. In classical kernel regression, the kernel itself encodes the inductive bias [Schölkopf and Smola, 2002], and a large body of work has investigated how different kernels shape generalization [Cucker and Smale, 2002, Györfi et al., 2002, Belkin et al., 2018b,a, 2019, Spigler et al., 2020]. In particular, Canatar et al. [2021], Bordelon and Pehlevan [2022] derived analytical characterizations of the generalization error for finite datasets and arbitrary kernels, revealing how spectral bias and code–task alignment govern kernel generalization.

State space models (SSMs) have recently emerged as effective architectures for modeling long sequences [Patro and Agneeswaran, 2025]. This includes not only LTI models but also powerful selective SSMs like Mamba, which adapt their parameters based on the input to achieve state-of-the-art performance. While empirically potent, the dynamic nature of these selective mechanisms makes them difficult to analyze formally. Our work provides the theoretical groundwork by focusing on the LTI case. A particular inductive bias of LTI SSMs, known as frequency bias, has drawn attention recently. Yu et al. [2024], Solozabal et al. [2025] analyzed and tuned this bias, achieving improved performance on the Long Range Arena benchmark [Tay et al., 2021], while Agarwal et al. [2024] proposed spectral initializations to better control frequency response. Beyond initialization, generalization and data-dependent training schemes for SSMs have also been studied [Liu and Li, 2024, 2025].

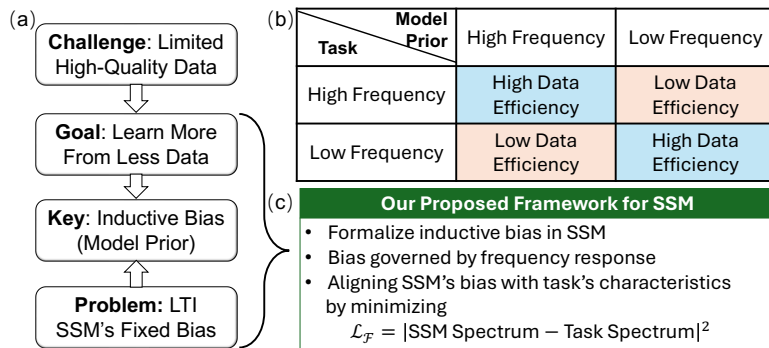


Figure 1: Conceptual figure. (a) To address the scarcity of high-quality data, improving data efficiency—learning more from less—is essential. A key lies in inductive bias (model prior), yet linear time-invariant (LTI) state space models (SSMs) encode fixed bias. (b) An illustrative table shows that data efficiency depends on the alignment between a model’s prior bias and the task. For instance, a high-frequency task matched with a high-frequency prior achieves higher data efficiency. (c) Our framework for SSMs: we first formalize inductive bias in LTI SSMs, which is governed by their inherent frequency response. We then introduce task-dependent initialization (TDI) to align model bias with task characteristics by minimizing a specific loss.

## 2 Preliminaries

### 2.1 Problem Statement

A challenge in machine learning is ensuring that a model generalizes well to unseen data. The generalization error,  $E_g$ , quantifies this ability by averaging the model's performance over all possible training datasets  $\mathcal{D}$  of a given size  $P$ . Formally, it is defined as  $E_g = \mathbb{E}_{\mathcal{D}}[E_g(\mathcal{D})]$ , where  $E_g(\mathcal{D}) = \mathbb{E}_{\mathbf{x}}[(f_{\mathcal{D}}^*(\mathbf{x}, \mathcal{D}) - \bar{f}(\mathbf{x}))^2]$  is the expected error on a new sample  $\mathbf{x}$  for a model  $f_{\mathcal{D}}^*$  trained on a specific dataset  $\mathcal{D}$ .

Models rely on an inductive bias—a set of built-in assumptions—to generalize effectively. For SSMs, this bias, particularly their inherent frequency bias, is poorly understood, which hinders principled analysis and generalization guarantees. This work bridges that gap with a kernel-theoretic framework that characterizes the spectral properties of SSMs. This formal characterization allows us to elucidate the model's inductive bias and develop a principled strategy to align it with the task, thereby improving data efficiency.

### 2.2 State Space Model and the Related Toeplitz Matrix as Linear Operators

Formally, a continuous-time linear time-invariant (LTI) state space model (SSM) is defined as

$$\dot{\mathbf{x}}(t) = \mathbf{A}\mathbf{x}(t) + \mathbf{B}\mathbf{u}(t), \quad \mathbf{y}(t) = \mathbf{C}\mathbf{x}(t) + \mathbf{D}\mathbf{u}(t), \quad (1)$$

where  $\mathbf{x}(t) \in \mathbb{R}^n$  denotes the hidden state,  $\mathbf{u}(t) \in \mathbb{R}^m$  is the input, and  $\mathbf{y}(t) \in \mathbb{R}^p$  is the output. We discretize the continuous SSM using the Zero-Order Hold (ZOH) method with step size  $\Delta$ , yielding the discrete SSM:

$$\mathbf{x}_{k+1} = \bar{\mathbf{A}}\mathbf{x}_k + \bar{\mathbf{B}}\mathbf{u}_k, \quad y_k = \bar{\mathbf{C}}\mathbf{x}_k, \quad (2)$$

where  $\bar{\mathbf{A}} = \exp(\Delta\mathbf{A})$ ,  $\bar{\mathbf{B}} = (\Delta\mathbf{A})^{-1}(\exp(\Delta\mathbf{A}) - \mathbf{I})\Delta\mathbf{B}$ ,  $\bar{\mathbf{C}} = \mathbf{C}$ . For simplicity, and in line with modern deep SSMs such as S4 [Gu et al., 2022a] and S4D [Gu et al., 2022b], we ignore the skip connection  $\mathbf{D}$  and treat  $u_k$  and  $y_k$  as scalars. For an initial state  $\mathbf{x}_{-1} = \mathbf{0}$ , the output sequence  $\{y_k\}$  is the convolution of the input sequence  $\{u_k\}$  with the SSM's impulse response kernel  $\bar{\mathbf{t}}$ , given by  $y_k = \sum_{n=0}^k \bar{\mathbf{t}}_n u_{k-n}$ , where the kernel is defined as  $\bar{\mathbf{t}}_n = \bar{\mathbf{C}}\bar{\mathbf{A}}^n\bar{\mathbf{B}}$ . The frequency response  $H(\omega)$  of an SSM is the discrete Fourier transform of its impulse response  $\bar{\mathbf{t}}$ ,  $H(\omega) = \text{DFT}(\bar{\mathbf{t}}) = \sum_{n=0}^{\infty} \bar{\mathbf{t}}_n e^{-i\omega n}$ ,  $\omega \in (0, 2\pi)$ . This convolutional process can be represented by a Toeplitz matrix  $\mathbf{T}_K$  that maps the entire input sequence  $\mathbf{u} = [u_0, \dots, u_{L-1}]^\top$  to the output sequence  $\mathbf{y} = [y_0, \dots, y_{L-1}]^\top$  through matrix multiplication  $\mathbf{y} = \mathbf{T}_K \mathbf{u}$ . The Toeplitz matrix  $\mathbf{T}_K$  is defined by  $\bar{\mathbf{t}}$  as follows:

$$\mathbf{T}_K = \begin{pmatrix} \bar{\mathbf{t}}_0 & 0 & 0 & \cdots & 0 \\ \bar{\mathbf{t}}_1 & \bar{\mathbf{t}}_0 & 0 & \cdots & 0 \\ \bar{\mathbf{t}}_2 & \bar{\mathbf{t}}_1 & \bar{\mathbf{t}}_0 & \cdots & 0 \\ \vdots & \vdots & \vdots & \ddots & \vdots \\ \bar{\mathbf{t}}_{L-1} & \bar{\mathbf{t}}_{L-2} & \bar{\mathbf{t}}_{L-3} & \cdots & \bar{\mathbf{t}}_0 \end{pmatrix}. \quad (3)$$

### 2.3 A Kernel-Theoretic Framework for Analyzing Inductive Bias

To analyze the inductive bias of SSMs, we employ the framework of kernel methods. Kernel Ridge Regression (KRR) provides a powerful lens for this by finding a function  $f$  in a Reproducing Kernel Hilbert Space (RKHS)  $\mathcal{H}_K$  that minimizes the regularized empirical risk:  $f_{\mathcal{D}}^* = \arg \min_{f \in \mathcal{H}_K} \frac{1}{P} \sum_{\mu=1}^P (f(\mathbf{x}^\mu) - \mathbf{y}^\mu)^2 + \lambda \|f\|_{\mathcal{H}_K}^2$ , where  $\lambda > 0$  is a regularization parameter,  $P$  is the number of training samples, and  $\mathcal{D} = \{\mathbf{x}^\mu, \mathbf{y}^\mu\}_{\mu=1}^P$  denotes the training set. The inputs  $\mathbf{x}^\mu$  are sampled i.i.d. from a distribution  $p(\mathbf{x})$ , and labels  $\mathbf{y}^\mu \in \mathbb{R}^d$  ( $d$  is the dimension of labels) are generated by  $\mathbf{y}^\mu = \bar{f}(\mathbf{x}^\mu) + \epsilon^\mu$ , where  $\epsilon^\mu$  are zero-mean noise with covariance  $\langle \epsilon^\mu \epsilon^\nu \rangle = \sigma^2 \delta_{\mu\nu}$ . The RKHS is uniquely defined by a kernel function  $K(\mathbf{x}, \mathbf{x}')$  that satisfies the reproducing property [Aronszajn, 1950, Schölkopf and Smola, 2002]. The spectral properties of the kernel, revealed by Mercer's Theorem, are crucial for understanding generalization.

**Theorem 2.1** (Mercer’s Theorem [Rasmussen and Williams, 2005]). *Let  $K(\mathbf{x}, \mathbf{x}')$  be a continuous, symmetric, and positive semi-definite kernel function. Then  $K$  can be decomposed as a series expansion in terms of its eigenfunctions  $\{\phi_\rho\}_{\rho=1}^\infty$  and non-negative eigenvalues  $\{\eta_\rho\}_{\rho=1}^\infty$ :  $K(\mathbf{x}, \mathbf{x}') = \sum_{\rho=1}^\infty \eta_\rho \phi_\rho(\mathbf{x}) \phi_\rho(\mathbf{x}')$ , where the eigenfunctions are normalized such that  $\int \phi_\rho(\mathbf{x}) \phi_{\rho'}(\mathbf{x}) p(\mathbf{x}) d\mathbf{x} = \delta_{\rho\rho'}$  with respect to a given distribution  $p(\mathbf{x})$ .*

The inductive bias of the kernel is encoded in its spectrum. As shown by Canatar et al. [2021], Bordelon and Pehlevan [2022], the generalization error can be decomposed into a sum of mode-wise errors. After expanding the target function  $\bar{f}(\mathbf{x}) = \sum_\rho \bar{w}_\rho \phi_\rho(\mathbf{x})$  and the learned function  $f^*(\mathbf{x}) = \sum_\rho w_\rho^* \phi_\rho(\mathbf{x})$  in the kernel’s eigenbasis, the total generalization error is  $E_g = \frac{1}{1-\gamma} \sum_\rho \frac{\kappa^2 \bar{w}_\rho^2 + \sigma^2 P \eta_\rho^2}{(\kappa + P \eta_\rho)^2}$ , where  $\kappa, \gamma$  are functions of the eigenvalues and sample size. This expression reveals a *spectral bias*: modes  $\rho$  corresponding to larger eigenvalues  $\eta_\rho$  are learned more rapidly as  $P$  increases.

The alignment between the task and the model’s bias can be quantified by the cumulative power,  $C(\rho) = \frac{\sum_{l=1}^\rho \bar{w}_l^2}{\sum_{l=1}^\infty \bar{w}_l^2}$ . Target functions whose power is concentrated in the top kernel modes (i.e., those with a fast-rising  $C(\rho)$ ) can be learned with fewer samples. For a  $d$ -dimensional target function, we set  $\bar{w}_\rho^2 = \sum_{j=1}^d \bar{w}_{\rho,j}^2$ , where each  $\bar{w}_{\rho,j}$  is defined by the expansion  $\bar{f}_j(\mathbf{x}) = \sum_\rho \bar{w}_{\rho,j} \phi_\rho(\mathbf{x})$ .

### 3 Methods

In this section, we first introduce our novel SSM-induced kernel (Section 3.1) and analyze its Reproducing Kernel Hilbert Space (RKHS), deriving its eigenvalues and eigenfunctions to characterize the associated spectral properties (Section 3.2). We then provide a sanity check to empirically validate these theoretical results in Section 3.3. Finally, we propose a task-dependent initialization method that aligns the SSM’s inductive bias with the task spectrum, and prove its effectiveness in enhancing generalization (Section 3.4).

#### 3.1 SSM-Induced Kernel

In Section 2.2, we established the link between a discrete-time SSM and its corresponding Toeplitz matrix  $\mathbf{T}_K$ , which maps an input sequence to an output sequence. We now leverage this connection to define a kernel function that models the behavior of the SSM. The perspective that views the Toeplitz matrix as a feature map allows us to analyze SSMs within the well-established framework of kernel methods.

**Definition 1** (SSM-Induced Kernel). *Let  $\mathbf{u}, \mathbf{u}' \in \mathbb{R}^L$  be two input sequences of length  $L$ . The SSM-induced kernel is defined as the inner product of their corresponding Toeplitz matrix features:  $K(\mathbf{u}, \mathbf{u}') = \frac{1}{L} (\mathbf{T}_K \mathbf{u})^\top (\mathbf{T}_K \mathbf{u}')$ , where  $\mathbf{T}_K$  denotes the Toeplitz matrix defined by the SSM’s impulse response kernel.*

The structure of the kernel is determined by the SSM parameters  $\mathbf{A}, \mathbf{B}, \mathbf{C}$ , and  $\Delta$ , which govern the temporal dynamics of the system. Unlike standard linear kernels that merely compute a dot product, the SSM-induced kernel captures temporal dependencies through its Toeplitz structure.

**Lemma 3.1** (Positive Semi-Definiteness). *The SSM-induced kernel  $K(\mathbf{u}, \mathbf{u}')$  is a valid kernel.*

The proof is available in Appendix C.1.

#### 3.2 Characterizing the SSM-Induced Kernel

After establishing the validity of the SSM-induced kernel (Lemma 3.1), we now study its RKHS. In particular, we will derive the eigenvalues and eigenfunctions of the kernel, which are crucial for understanding the kernel’s spectral properties and their impact on generalization.

We begin by considering the singular value decomposition (SVD) of  $\mathbf{T}_K \in \mathbb{R}^{L \times L}$ ,  $\mathbf{T}_K = \sqrt{L} \mathbf{U} \mathbf{S} \mathbf{V}^\top$ , where  $\mathbf{S} = \text{diag}\{s_1, \dots, s_L\}$  are the singular values,  $\mathbf{V}^\top$  is the right singular matrix, and  $\sqrt{L}$  is a scale factor. Inserting SVD results of  $\mathbf{T}_K$  into Definition 1, the kernel  $K(\mathbf{u}, \mathbf{u}')$  can be expressed as  $K(\mathbf{u}, \mathbf{u}') = (\mathbf{V}^\top \mathbf{u})^\top \mathbf{S}^2 (\mathbf{V}^\top \mathbf{u}')$ . To connect the Toeplitz matrix with the RKHS of our kernel, we make the following assumption about the data distribution. This assumption is

common in theoretical analyses and can be achieved through data whitening [Kessy et al., 2018]. Under this assumption, the rows  $\mathbf{V}^\top \mathbf{u}$  form a set of orthonormal eigenfunctions.

**Assumption 1.** *We assume that the input sequences  $\mathbf{u}$  are sampled i.i.d. from a distribution with a zero mean and a covariance of  $\mathbb{E}_{\mathbf{u}}[\mathbf{u}\mathbf{u}^\top] = \mathbf{I}_L$ .*

**Lemma 3.2** (Orthonormal Eigenfunctions). *Under Assumption 1, rows of  $\mathbf{V}^\top \mathbf{u}$  form a set of orthonormal eigenfunctions for the SSM-induced kernel.*

The proof of Lemma 3.2 is in Appendix C.1. Combining Theorem 2.1, Lemma 3.1 and Lemma 3.2, we derive the eigen-decomposition of our SSM-induced kernel.

**Theorem 3.3** (Eigen-Decomposition of SSM-Induced Kernel). *Under Assumption 1, given the Toeplitz matrix  $\mathbf{T}_K \in \mathbb{R}^{L \times L}$ , the SSM-induced kernel has a rank at most  $L$ , and its eigen-decomposition is determined by  $K(\mathbf{u}, \mathbf{u}') = \sum_{\rho} \eta_{\rho} \phi_{\rho}(\mathbf{u}) \phi_{\rho}(\mathbf{u}')$ , where  $\eta_{\rho} = s_{\rho}^2$ ,  $\phi_{\rho}(\mathbf{u}) = (\mathbf{V}^\top \mathbf{u})_{\rho}$ , for  $\rho = 1, \dots, L$ .*

The finite rank of the kernel follows directly from the fact that it is induced by a finite-dimensional feature map. Therefore, all eigenvalues  $\eta_{\rho}$  for  $\rho > L$  are zero.

The spectral bias of our SSM-induced kernel arises from the connection between its singular values and the model’s frequency response. As discussed in Section 2, modes  $\rho$  with larger eigenvalues  $\eta_{\rho}$  are learned faster as the sample size  $P$  increases. For our kernel, these eigenvalues are given by the squared singular values of the associated Toeplitz matrix,  $\eta_{\rho} = s_{\rho}^2$ . This ordering directly induces a spectral bias, reflecting the model’s preference for learning certain frequency components more rapidly. Importantly, we show that this spectral bias is governed by the SSM’s frequency response  $|H(\omega)|$ . Appendix E formally establishes the connection between the singular values of  $\mathbf{T}_K$  and the frequency response, summarized in Theorem 3.4. Thus, the inductive bias of the kernel (or of SSM) is actually its frequency bias, because large  $s_{\rho}$  indicates a strong frequency response at  $\omega_{\rho}$ .

**Theorem 3.4.** *Under Assumption 1, the relationship between the singular values of  $\mathbf{T}_K$  and the frequency response  $|H(\omega)|$  of SSM is simply  $s_{\rho} = |H(\omega_{\rho})|$ , where  $\omega_{\rho} = \frac{2\pi\rho}{L}$  ( $\rho = 0, \dots, L-1$ ). Note that  $s_{\rho}$  is not sorted here.*

While we assume a unit input covariance for simplicity, our main results can be generalized. For a general input covariance  $\mathbb{E}_{\mathbf{u}}[\mathbf{u}\mathbf{u}^\top] = \Sigma$ , we reparameterize the input as  $\mathbf{x} = \Sigma^{-\frac{1}{2}}\mathbf{u}$ , which ensures  $\mathbb{E}[\mathbf{x}\mathbf{x}^\top] = \mathbf{I}_L$ . Then, the original Toeplitz map  $\mathbf{T}_K \mathbf{u}$  is equivalent to  $\tilde{\mathbf{T}}\mathbf{x}$  where  $\tilde{\mathbf{T}} = \mathbf{T}_K \Sigma^{\frac{1}{2}} = \sqrt{L} \tilde{\mathbf{U}} \tilde{\mathbf{S}} \tilde{\mathbf{V}}^\top$ . This modified SVD result determines the eigen-decomposition by  $\eta_{\rho} = \tilde{s}_{\rho}^2$ ,  $\phi_{\rho}(\mathbf{u}) = (\tilde{\mathbf{V}}^\top \Sigma^{-\frac{1}{2}} \mathbf{u})_{\rho}$ , for  $\rho = 1, \dots, L$ . While  $\tilde{s}_{\rho}$  does not admit a closed-form expression, Appendix E demonstrates that  $s_{\rho}$  is strongly associated with the degree of alignment between the SSM and the data. Our analysis indicates that greater alignment leads to larger values of  $s_{\rho}$ , thereby accelerating the learning dynamics of  $\phi_{\rho}$ .

Though the eigen-decomposition of the SSM-induced kernel is mathematically straightforward, it provides a powerful, non-trivial tool for analyzing the kernel. This decomposition directly reveals the system’s inductive bias by characterizing the spectrum and identifying the eigenfunctions that govern its behavior.

### 3.3 Empirical Validation of the Kernel’s Eigen-Decomposition

As a sanity check, we empirically validate the eigen-decomposition result of the SSM-induced kernel (Theorem 3.3) on 15,000 randomly selected MNIST images [Deng, 2012]. Results are shown in Figure 2. We empirically validate our theoretical predictions on whitened data. As the effective dimensions decrease after data whitening, we reduced MNIST to 550 dimensions. Figure 2(a) shows that the empirical eigenvalues with index  $\rho < L$  closely match the theoretical predictions. Moreover, theoretical and empirical eigenvectors agree strongly, with the relative error remaining close to zero across most modes (Figure 2(b)), as well as the squared weights  $\bar{w}_{\rho}^2$  (Figure 2(c)). These results demonstrate that our theory successfully captures the spectral characteristics of the

SSM-induced kernel. Additional figures including the spectrum, relative error, and squared weights on unwhitened data can be found in Appendix B.1.

In Figure 2(d), we further compare the theoretical and empirical cumulative power curves for both whitened (green) and unwhitened (red) data. In both cases, theory aligns well with experiment. Notably, the cumulative power  $C(\rho)$  for unwhitened data grows more rapidly than that of whitened data, which in turn leads to improved generalization performance, as shown in Figure 2(e). This difference reflects the inevitable loss of information induced by the whitening procedure.

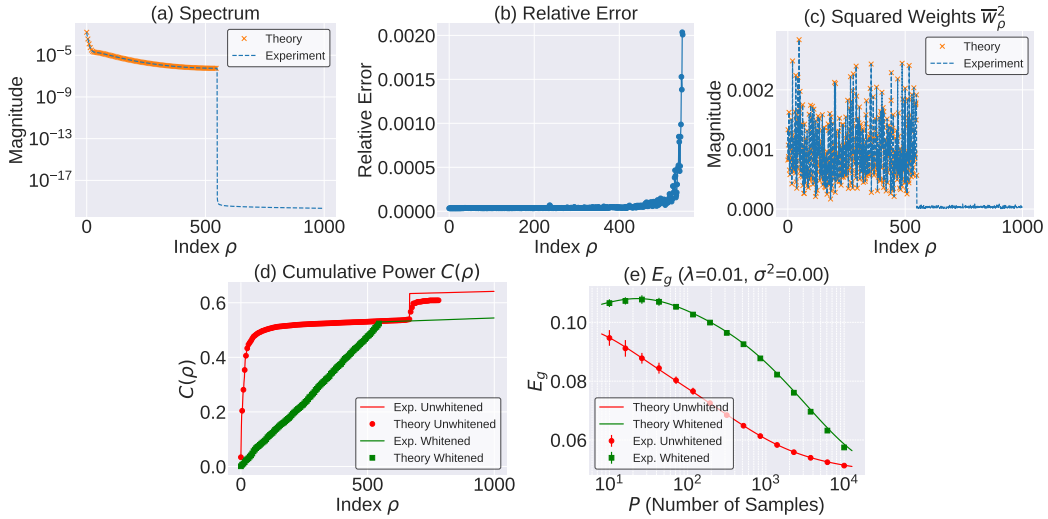


Figure 2: Empirical validation of the eigen-decomposition of the SSM-induced kernel. (a) Spectrum: empirical (blue dashed) vs. theoretical (orange crosses) eigenvalues on whitened data. (b) Relative error between empirical and theoretical eigenvectors. (c) Squared weights of empirical vs. theoretical eigenfunctions. (d) Cumulative power on unwhitened (red) vs. whitened (green) data. (e) Generalization error: models trained on unwhitened (red) vs. whitened (green) data. Error bars indicate the standard deviation over 50 independent runs. Solid lines are calculated by Canatar et al. [2021]’s theory (Section 2). The empirical spectrum of the SSM kernel aligns with our theoretical predictions (Theorem 3.3).

It is worth noting that while Theorem 3.3 states that the kernel’s rank is at most  $L$ , in our empirical results, the eigenvalues for  $\rho > L$  are not strictly zero due to numerical and empirical noise (Figure 2(a)). Although these eigenvalues are small, their effect on the power curve is non-negligible. This can be observed in Figure 2(d), where the cumulative power curve continues to increase even after the initial  $L$  modes, indicating that the tail eigenvalues act as effective noise. The phenomenon is also found in Canatar et al. [2021, 2022], Simon et al. [2023], which explains why the green curve is not monotonically decreasing in Figure 2(e).

### 3.4 Designing SSM Parameter via Task-Dependent Initialization

In this section, we present a novel method to optimize the SSM parameters by aligning the model’s inductive bias with the frequency spectral characteristics of the task. Our goal is to shape the SSM’s power spectrum to match that of the task, thereby aligning the model’s top eigenbasis with the target function.

Concretely, our method seeks to align two quantities in the frequency domain: the model power spectrum  $|H(\omega)|^2$  derived from the SSM’s intrinsic frequency response and the task power spectrum  $G_{\mathbf{u}\mathbf{y}}(\omega)$  estimated from the Fourier transform of the input-output cross-variance matrix  $\mathbf{C}_{\mathbf{u}\mathbf{y}} = \mathbb{E}_{\mathbf{u}}[\mathbf{u}\mathbf{y}^\top] \approx \frac{1}{P} \sum_{\mu=1}^P \mathbf{u}^\mu \mathbf{y}^{\mu\top}$ . To formalize this alignment, we introduce the following loss.

**Definition 2** (Power Spectrum Matching Loss). *We define the power spectrum matching loss  $\mathcal{L}_F$  as the squared  $L_2$ -distance between the normalized model and task power spectra:*

$$\mathcal{L}_F = \left\| \frac{|H(\omega)|^2}{\| |H(\omega)|^2 \|_2} - \frac{|G_{\mathbf{u}\mathbf{y}}(\omega)|}{\| |G_{\mathbf{u}\mathbf{y}}(\omega)| \|_2} \right\|_2^2, \quad (4)$$

where  $|G_{\mathbf{u}\mathbf{y}}(\omega)|$  denotes the magnitude of the task’s cross-power spectral density, given by  $|\mathcal{F}(\mathbf{C}_{\mathbf{u}\mathbf{y}})|$ , averaged across the label dimension  $d$ .

The power spectrum matching loss provides a direct criterion to measure how well the SSM’s frequency response aligns with the task. The SSM parameters are then optimized via gradient descent to minimize this loss. Since  $G_{\mathbf{u}\mathbf{y}}(\omega)$  identifies the frequencies at which the input signal most effectively drives the output of the task [Smith, 2007], it is intuitive to shape the SSM’s power spectrum to align with it.

We provide a two-part theoretical justification of this method. First, we show that maximizing a general alignment objective  $J$ , promotes a rapid increase in  $C(\rho)$  (Lemma 3.5). Then we show that minimizing power spectrum matching loss  $\mathcal{L}_F$  is an efficient strategy for maximizing  $J$  (Lemma 3.6).

**Lemma 3.5.** *Maximizing a general alignment objective  $J = K(\mathbf{C}_{\mathbf{u}\mathbf{y}}, \mathbf{C}_{\mathbf{u}\mathbf{y}}) \equiv \frac{1}{L} \|\mathbf{T}_K \mathbf{C}_{\mathbf{u}\mathbf{y}}\|_F^2$  promotes a rapid increase in  $C(\rho)$ , where  $\|\cdot\|_F$  denotes the Frobenius norm.*

**Lemma 3.6.** *Minimizing power spectrum matching loss  $\mathcal{L}_F$  is equivalent to maximizing  $J$ .*

The proofs of Lemma 3.5 and Lemma 3.6 can be found in Appendix C.2. Based on Lemma 3.5 and Lemma 3.6, we obtain our final theorem.

**Theorem 3.7** (Power Spectrum Matching Improves Generalization Ability). *Minimizing power spectrum matching loss  $\mathcal{L}_F$  promotes a rapid increase in  $C(\rho)$ , thus improving the generalization ability of SSM-induced kernel by aligning its inductive bias with the task’s frequency spectral properties.*

We term this method **Task-Dependent Initialization (TDI)**, since it directly utilizes the power spectrum of the task to initialize the model’s inductive bias. The detailed algorithm and implementation are provided in the Appendix D.3.

## 4 Experiments

In this section, we first demonstrate that our method of TDI via power spectrum matching effectively promotes faster growth of cumulative power and improves generalization by aligning the SSM’s inductive bias with task characteristics (Section 4.1). Then, we extend our method to deep learning models, showing that aligning their spectral inductive bias with task properties leads to consistently improved generalization performance (Section 4.2).

### 4.1 Power Spectrum Matching Improves Generalization

We validate the TDI method from Section 3.4, which increases cumulative power  $C(\rho)$  by optimizing SSM parameters via gradient descent on the power spectrum matching loss  $\mathcal{L}_F$ . We choose S4D initialization [Gu et al., 2022b] as our initial SSM parameters due to its simplicity and explainability.

We conduct our experiments on synthetic data. In the first set of experiments, we consider a low-frequency task. We track the evolution of  $C(\rho)$  and the learning curve across iterations starting from S4D initialization. In the second set of experiments, we consider a high-frequency task and use the same S4D initialization as the low-frequency task. The results are shown in Figure 3 (low-frequency task) and Figure 4 (high-frequency task). Details of the experiments are available in Appendix D.2.

For low-frequency tasks, the SSM’s initial power spectrum is already close to that of the task, so gradient descent induces minimal changes (Figure 3(a)), reflected in nearly overlapping cumulative

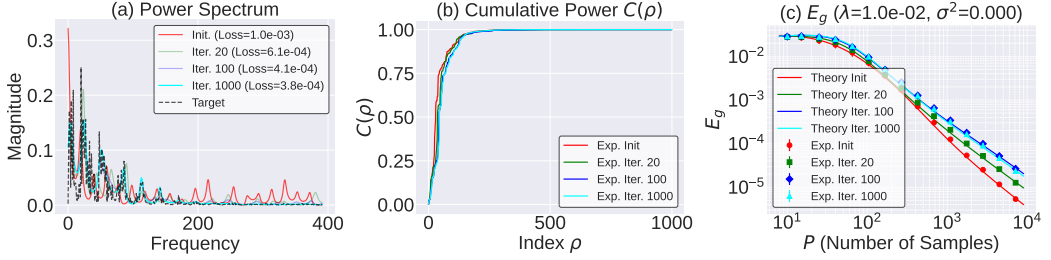


Figure 3: Experiments on synthetic data (low frequency). (a) Power spectrum of the target and SSM at different training iterations. (b) Cumulative power  $C(\rho)$ . (c) Generalization error  $E_g$ . Error bars indicate the standard deviation over 50 independent runs. Colored lines denote different optimization iterations, while the black dashed line indicates the target spectrum. For the low-frequency task, the cumulative power and learning curves remain nearly unchanged across iterations.

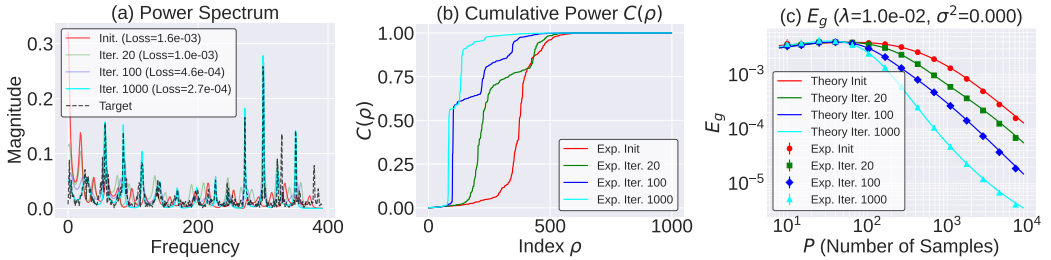


Figure 4: Experiments on synthetic data (high frequency). Panels (a–c) are analogous to those in Figure 3. For this high-frequency task, the SSM’s power spectrum evolves markedly during gradient descent, as seen in the cumulative power and learning curves. Power spectrum matching accelerates the growth of  $C(\rho)$  and improves generalization.

power curves  $C(\rho)$  (Figure 3(b)) and learning curves (Figure 3(c)). In fact, the matching process may slightly impair generalization performance. Conversely, for high-frequency tasks, the initial power spectrum of the SSM differs substantially from that of the task, leading to significant spectral changes during optimization (Figure 4(a)). As a result,  $C(\rho)$  rises more rapidly toward 1 (Figure 4(b)), and generalization is improved markedly during optimization (Figure 4(c)). The learning curves under more parameter settings can be found in Appendix B.2, demonstrating the generality of our results.

Although the initial spectrum is closer to low-frequency tasks, this does not imply an inherent low-frequency bias as defined in Yu et al. [2024], i.e., the frequency response has more variation in the low-frequency area. We analyze the frequency bias of an S4D-like SSM in Appendix F, showing its direct relation to the SSM parameters (Theorem F.1). We also construct an SSM with low-frequency bias and another with high-frequency bias and test them on both the low- and high-frequency tasks. The results (see Appendix B.3 for details) show (1) SSMs do not always encode low-frequency bias; (2) an appropriate frequency bias is crucial for good generalization, as it ensures a low power spectrum matching loss and facilitates subsequent optimization.

## 4.2 Application to Deep Learning Models

Then, we apply TDI to deep SSMs and evaluate them on real-world benchmark datasets. We train the models on a diverse set of benchmark tasks, including CIFAR-10 [Krizhevsky and Hinton, 2009], Pathfinder [Tay et al., 2021], and ListOps [Nangia and Bowman, 2018] from the LRA suite, as well as Speech Commands [Warden, 2018]. The baseline and TDI models share identical hyperparameters and both adopt the S4D architecture, with the only difference being that the first S4 layer of the TDI model is optimized via power spectrum matching. To assess the effectiveness

of our method across different data regimes, we vary the size of the training set while keeping the sizes of validation and test sets fixed, and report the median test loss over 5 random seeds. For each epoch, we obtain a learning curve of test loss versus training data fraction. To reduce redundancy and variance, we average test losses over non-overlapping windows of 10–15 epochs and plot these aggregated results. Hyperparameter settings and other details are available in Appendix D.5. For completeness, the detailed training curves (loss versus epoch at each ratio) are included in Appendix B.5.

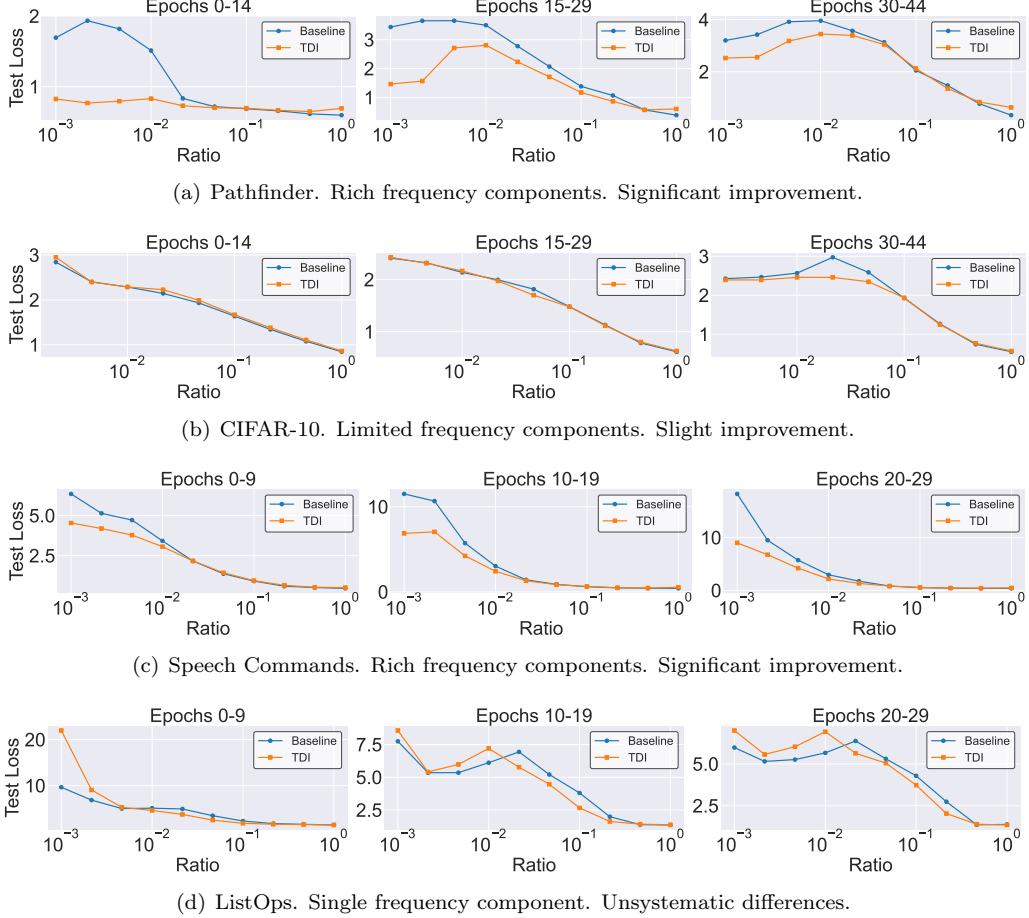


Figure 5: Test loss of the baseline SSM (blue) and our proposed TDI model (orange) across different training data ratios. Each marker denotes the test loss obtained by first taking the median across 5 random seeds at each epoch, and then averaging these epoch-wise medians over non-overlapping windows of 10 (or 15) consecutive epochs. The effectiveness of TDI is closely related to the spectral properties of the task. Additional power spectrum figures for these datasets are shown in Appendix B.4.

As shown in Figure 5(a), our method achieves lower test losses across almost all data ratios for the Pathfinder task. The improvement is most pronounced in the low-ratio regime, where the aligned inductive bias plays a crucial role. This finding supports our theory that TDI improves generalization, which is further corroborated by the results on Speech Commands (Figure 5(c)). In contrast, the improvement on CIFAR-10 is relatively small (Figure 5(b)), and that on ListOps is marginal (Figure 5(d)). Overall, these results suggest that the effectiveness of TDI is closely tied to the spectral properties of the task: tasks with richer frequency components, especially those dominated by high frequencies (e.g., Pathfinder, Speech Commands), benefit more from spectrum matching than those with weaker or low-frequency structures (e.g., CIFAR-10, ListOps). Since the original S4 model already incorporates a low-frequency bias (see Appendix F), the improvement on low-frequency tasks is limited. This observation is consistent with that in Section 4.1. We further

illustrate the frequency properties of these datasets in Appendix B.4, which shows Pathfinder and Speech Commands contain stronger spectral components, particularly at high frequencies compared to CIFAR-10, and across all frequencies compared to ListOps, confirming the interpretation above.

## 5 Conclusions

This work addressed the challenge of data efficiency by formalizing and optimizing the inductive bias of LTI State Space Models. We began by establishing a rigorous theoretical foundation, which directly motivated the development of TDI, a practical and efficient method that aligns the model’s initial inductive bias with the task’s unique spectral characteristics. Our empirical validation on a diverse set of real-world benchmarks demonstrated that TDI significantly enhances data-efficient generalization. Crucially, our framework also explains why gains are marginal on tasks where the default model bias is already well-aligned, reinforcing the predictive power of our spectral analysis.

While this work provides a robust solution for the important class of LTI SSMs, its scope defines clear directions for future inquiry. First, our theoretical framework is rooted in the LTI assumption, which underpins the entire class of SSMs, making its extension to dynamic, selective architectures like Mamba the most critical next step. Second, our current analysis is focused on one-dimensional scalar sequences  $\{u_k\}$ . Extending our formulation and the TDI method to handle high-dimensional inputs represents a key challenge for future work. Third, we have only applied TDI to the first layer of the SSM; a natural extension is to explore strategies for multi-layer task-dependent initialization. Finally, the benefits of TDI are most pronounced on spectrally-rich tasks, clarifying its domain of applicability and highlighting that it is not a universal solution for all sequence problems.

## References

Amina Adadi. A survey on data-efficient algorithms in big data era. *Journal of Big Data*, 8(1):24, 2021.

Naman Agarwal, Daniel Suo, Xinyi Chen, and Elad Hazan. Spectral state space models. In *First Workshop on Long-Context Foundation Models@ ICML 2024*, 2024.

Nachman Aronszajn. Theory of reproducing kernels. *Transactions of the American mathematical society*, 68(3):337–404, 1950.

Yasaman Bahri, Ethan Dyer, Jared Kaplan, Jaehoon Lee, and Utkarsh Sharma. Explaining neural scaling laws. *Proceedings of the National Academy of Sciences*, 121(27):e2311878121, 2024.

Peter W Battaglia, Jessica B Hamrick, Victor Bapst, Alvaro Sanchez-Gonzalez, Vinicius Zambaldi, Mateusz Malinowski, Andrea Tacchetti, David Raposo, Adam Santoro, Ryan Faulkner, et al. Relational inductive biases, deep learning, and graph networks. *arXiv preprint arXiv:1806.01261*, 2018.

Mikhail Belkin, Daniel J Hsu, and Partha Mitra. Overfitting or perfect fitting? risk bounds for classification and regression rules that interpolate. *Advances in neural information processing systems*, 31, 2018a.

Mikhail Belkin, Siyuan Ma, and Soumik Mandal. To understand deep learning we need to understand kernel learning. In *International conference on machine learning*, pages 541–549. PMLR, 2018b.

Mikhail Belkin, Alexander Rakhlin, and Alexandre B Tsybakov. Does data interpolation contradict statistical optimality? In *The 22nd international conference on artificial intelligence and statistics*, pages 1611–1619. PMLR, 2019.

Blake Bordelon and Cengiz Pehlevan. Population codes enable learning from few examples by shaping inductive bias. *eLife*, 11:e78606, dec 2022. ISSN 2050-084X. doi: 10.7554/eLife.78606. URL <https://doi.org/10.7554/eLife.78606>.

Abdulkadir Canatar, Blake Bordelon, and Cengiz Pehlevan. Spectral bias and task-model alignment explain generalization in kernel regression and infinitely wide neural networks. *Nature communications*, 12(1):1–12, 2021.

Abdulkadir Canatar, Evan Peters, Cengiz Pehlevan, Stefan M. Wild, and Ruslan Shaydulin. Band-width enables generalization in quantum kernel models. *Trans. Mach. Learn. Res.*, 2023, 2022. URL <https://api.semanticscholar.org/CorpusID:249642463>.

Gui Citovsky, Giulia DeSalvo, Claudio Gentile, Lazaros Karydas, Anand Rajagopalan, Afshin Ros-tamizadeh, and Sanjiv Kumar. Batch active learning at scale. *Advances in Neural Information Processing Systems*, 34:11933–11944, 2021.

Cucker and Smale. Best choices for regularization parameters in learning theory: On the bias—variance problem. *Foundations of computational Mathematics*, 2(4):413–428, 2002.

Tri Dao and Albert Gu. Transformers are SSMs: Generalized models and efficient algorithms through structured state space duality. In *International Conference on Machine Learning (ICML)*, 2024.

Li Deng. The mnist database of handwritten digit images for machine learning research [best of the web]. *IEEE Signal Processing Magazine*, 29(6):141–142, 2012. doi: 10.1109/MSP.2012.2211477.

Anirudh Goyal and Yoshua Bengio. Inductive biases for deep learning of higher-level cognition. *Proceedings of the Royal Society A*, 478(2266):20210068, 2022.

Robert M Gray et al. Toeplitz and circulant matrices: A review. *Foundations and Trends® in Communications and Information Theory*, 2(3):155–239, 2006.

Albert Gu and Tri Dao. Mamba: Linear-time sequence modeling with selective state spaces. *arXiv preprint arXiv:2312.00752*, 2023.

Albert Gu, Karan Goel, and Christopher Ré. Efficiently modeling long sequences with structured state spaces. In *The International Conference on Learning Representations (ICLR)*, 2022a.

Albert Gu, Ankit Gupta, Karan Goel, and Christopher Ré. On the parameterization and initialization of diagonal state space models. *Advances in Neural Information Processing Systems*, 35, 2022b.

László Györfi, Michael Kohler, Adam Krzyżak, and Harro Walk. *A distribution-free theory of nonparametric regression*. Springer, 2002.

Trevor Hastie, Robert Tibshirani, Jerome Friedman, et al. The elements of statistical learning, 2009.

Joel Hestness, Sharan Narang, Newsha Ardalani, Gregory Diamos, Heewoo Jun, Hassan Kianinejad, Md Mostafa Ali Patwary, Yang Yang, and Yanqi Zhou. Deep learning scaling is predictable, empirically. *arXiv preprint arXiv:1712.00409*, 2017.

Jared Kaplan, Sam McCandlish, Tom Henighan, Tom B Brown, Benjamin Chess, Rewon Child, Scott Gray, Alec Radford, Jeffrey Wu, and Dario Amodei. Scaling laws for neural language models. *arXiv preprint arXiv:2001.08361*, 2020.

Agnan Kessy, Alex Lewin, and Korbinian Strimmer. Optimal whitening and decorrelation. *The American Statistician*, 72(4):309–314, January 2018. ISSN 1537-2731. doi: 10.1080/00031305.2016.1277159. URL <http://dx.doi.org/10.1080/00031305.2016.1277159>.

Alex Krizhevsky and Geoffrey Hinton. Learning multiple layers of features from tiny images. Technical Report 0, University of Toronto, Toronto, Ontario, 2009. URL <https://www.cs.toronto.edu/~kriz/learning-features-2009-TR.pdf>.

Fusheng Liu and Qianxiao Li. From generalization analysis to optimization designs for state space models. In *Proceedings of the 41st International Conference on Machine Learning*, ICML’24. JMLR.org, 2024.

Fusheng Liu and Qianxiao Li. Autocorrelation matters: Understanding the role of initialization schemes for state space models. In *The Thirteenth International Conference on Learning Representations*, 2025.

Nikita Nangia and Samuel R Bowman. Listops: A diagnostic dataset for latent tree learning. *arXiv preprint arXiv:1804.06028*, 2018.

Badri Narayana Patro and Vijay Srinivas Agneeswaran. Mamba-360: Survey of state space models as transformer alternative for long sequence modelling: Methods, applications, and challenges. *Engineering Applications of Artificial Intelligence*, 159:111279, 2025.

Carl Edward Rasmussen and Christopher K. I. Williams. *Gaussian Processes for Machine Learning*. The MIT Press, 11 2005. ISBN 9780262256834. doi: 10.7551/mitpress/3206.001.0001. URL <https://doi.org/10.7551/mitpress/3206.001.0001>.

Bernhard Schölkopf and Alexander J Smola. *Learning with kernels: support vector machines, regularization, optimization, and beyond*. MIT press, 2002.

Connor Shorten and Taghi M Khoshgoftaar. A survey on image data augmentation for deep learning. *Journal of big data*, 6(1):1–48, 2019.

James B Simon, Madeline Dickens, Dhruva Karkada, and Michael R DeWeese. The eigenlearning framework: A conservation law perspective on kernel ridge regression and wide neural networks. *Transactions on Machine Learning Research*, 2023.

Jimmy TH Smith, Andrew Warrington, and Scott W Linderman. Simplified state space layers for sequence modeling. In *ICLR*, 2023.

Julius O. Smith. *Mathematics of the Discrete Fourier Transform (DFT)*. W3K Publishing, <http://www.w3k.org/books/>, 2007. ISBN 978-0-9745607-4-8.

Ruben Solozabal, Velibor Bojkovic, Hilal AlQuabeh, Kentaro Inui, and Martin Takáč. Uncovering the spectral bias in diagonal state space models. *arXiv preprint arXiv:2508.20441*, 2025.

Stefano Spigler, Mario Geiger, and Matthieu Wyart. Asymptotic learning curves of kernel methods: empirical data versus teacher–student paradigm. *Journal of Statistical Mechanics: Theory and Experiment*, 2020(12):124001, 2020.

Chen Sun, Abhinav Shrivastava, Saurabh Singh, and Abhinav Gupta. Revisiting unreasonable effectiveness of data in deep learning era. In *Proceedings of the IEEE international conference on computer vision*, pages 843–852, 2017.

Yi Tay, Mostafa Dehghani, Samira Abnar, Yikang Shen, Dara Bahri, Philip Pham, Jinfeng Rao, Liu Yang, Sebastian Ruder, and Donald Metzler. Long range arena : A benchmark for efficient transformers. In *International Conference on Learning Representations*, 2021. URL <https://openreview.net/forum?id=qVyeW-grC2k>.

Pete Warden. Speech commands: A dataset for limited-vocabulary speech recognition. *arXiv preprint arXiv:1804.03209*, 2018.

Annan Yu, Dongwei Lyu, Soon Hoe Lim, Michael W Mahoney, and N Benjamin Erichson. Tuning frequency bias of state space models. In *The Thirteenth International Conference on Learning Representations*, 2024.

## A The Use of Large Language Models (LLMs)

We disclose the use of Large Language Models (LLMs) in our work.

- **Language polishing.** LLMs are used to improve grammar, style, and clarity of writing.

- **Literature discovery.** LLMs are used as a retrieval and discovery tool to help identify potentially relevant prior works. All cited references, however, are carefully verified and selected by the authors.

The intellectual contributions, including problem formulation, theoretical analysis, algorithm design, and experimental work, are solely those of the authors.

## B Additional Figures

### B.1 Validation of the Kernel’s Eigen-Decomposition on Unwhitened Data

This section provides additional figures for Section 3.3, including the spectrum, relative error and squared weights analyzed on unwhitened data. We also provide the comparison of theoretical and

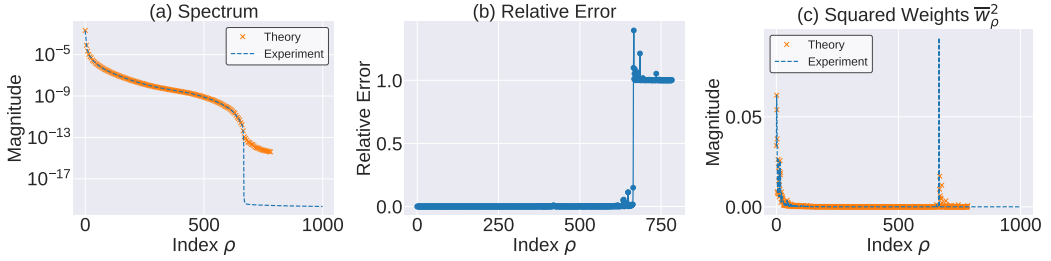


Figure B.1: Empirical validation of the SSM-induced kernel on unwhitened data. (a) Spectrum: empirical (blue dashed) vs. theoretical (orange crosses) eigenvalues on unwhitened data. (b) Relative error between empirical and theoretical eigenvectors. (c) Squared weights of empirical vs. theoretical eigenfunctions.

empirical top eigenvectors. As shown in Figure B.1 and Figure B.2, theory and experiment are in strong agreement.

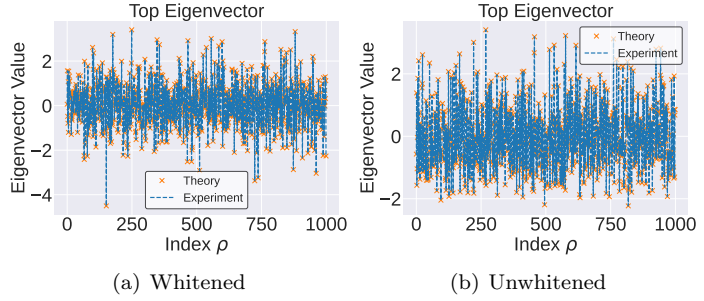


Figure B.2: Comparison of theoretical (orange crosses) and empirical (blue dashed) top eigenvectors. (a) Top eigenvector of whitened data. (b) Top eigenvector of unwhitened data.

### B.2 Learning Curves under More Parameter Settings

This section provides additional figures for Section 4.1, including learning curves under more parameter settings, shown in Figure B.3 and Figure B.4.

Consistent with Section 4.1, learning curves of the low-frequency task remain stable, while those of the high-frequency task evolve substantially during optimization. We also note that with noise  $\sigma^2 > 0$ , the light blue curve exhibits larger errors under small-sample conditions ( $P \sim 100$ ) compared to the others (Figure B.4). Because SSM parameters are tuned to high frequencies, the model confuses high-frequency signals with noise under small-sample conditions.

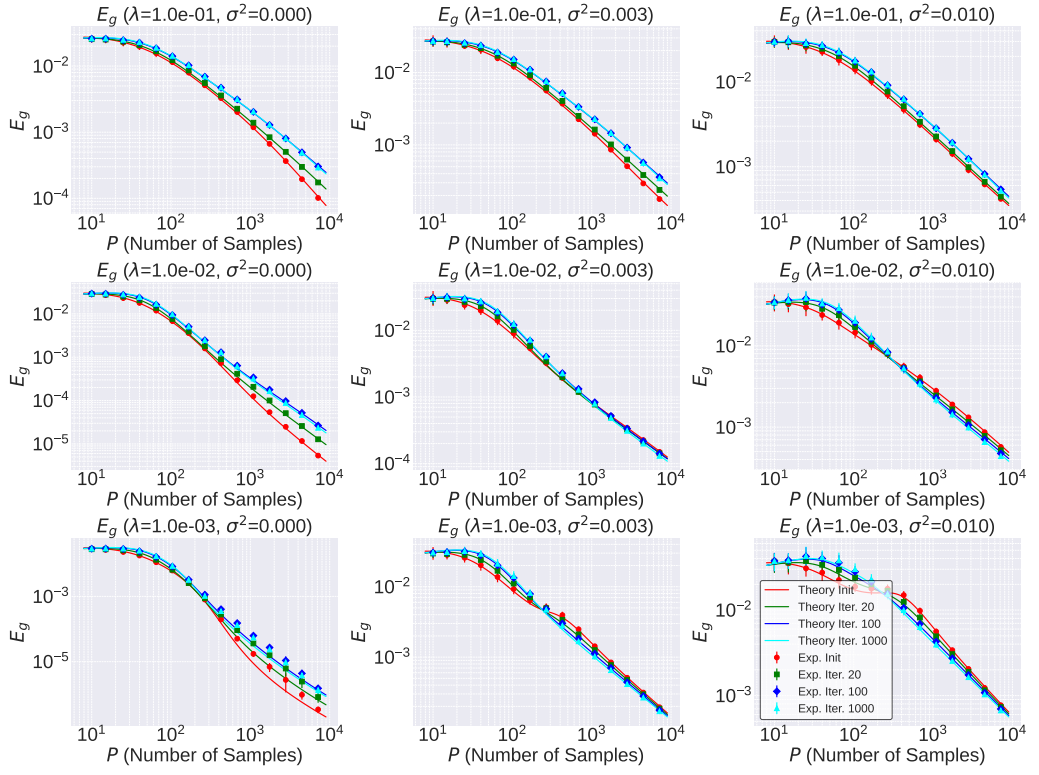


Figure B.3: Learning curves of low-frequency task under more parameter settings.

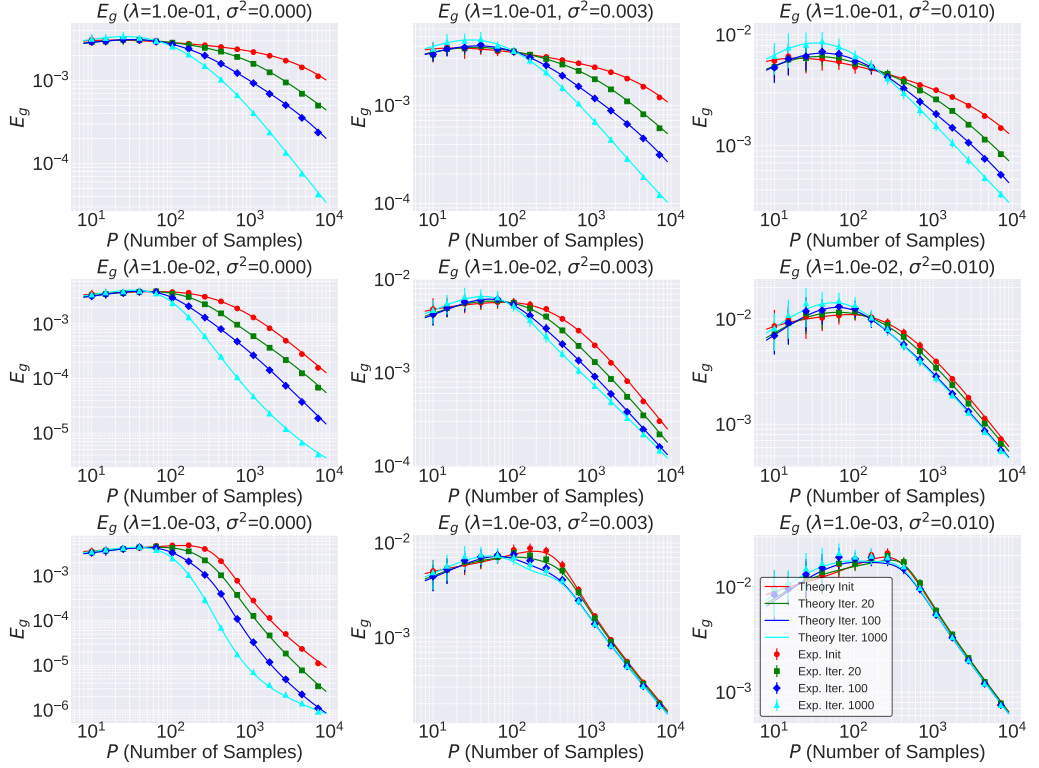


Figure B.4: Learning curves of high-frequency task under more parameter settings.

### B.3 SSMs with Low- and High-Frequency Bias

We construct two SSMs, one with low-frequency bias and another with high-frequency bias (see Appendix D.4 for construction details), and test them on both low- and high-frequency tasks. The results are shown in Figure B.5 and Figure B.6. One key observation is that the two

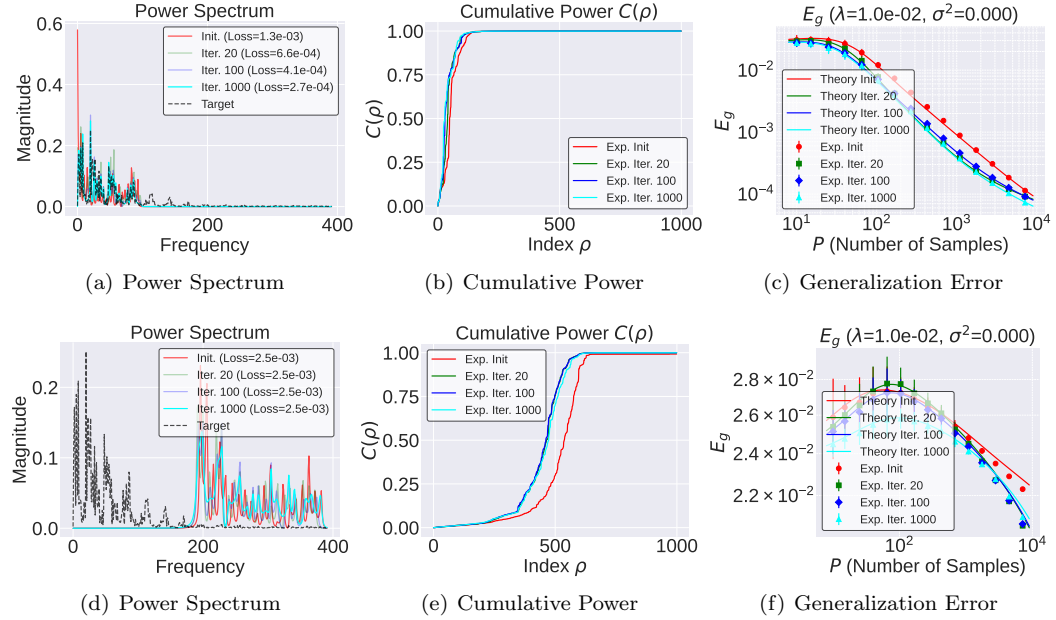


Figure B.5: Comparison on low-frequency task. (a-c): Power spectrum, cumulative power curves and learning curves of low-frequency SSM. (d-f): Power spectrum, cumulative power curves and learning curves of high-frequency SSM. Colored lines denote different optimization iterations, while the black dashed line indicates the target spectrum.

SSMs exhibit completely different properties. The initial power spectrum of low-frequency SSM is almost concentrated in the low-frequency range (Figure B.5(a), Figure B.6(a)), while that of high-frequency SSM is the opposite (Figure B.5(d), Figure B.6(d)). The distinct initial states steer optimization toward distinct outcomes. When the initial power spectrum poses a correct guess, SSM parameters are learned toward the right solution, resulting in faster-rising  $C(\rho)$  and better generalization performance (Figure B.5(b-c), Figure B.6(e-f)), while a bad initialization results in an incorrect spectrum, slower-rising  $C(\rho)$  and poorer generalization (Figure B.5(e-f), Figure B.6(b-c)). The results suggest that an appropriate initialization of the SSM parameters, and correspondingly an appropriate frequency bias, is crucial for good generalization.

Additionally, it is observed that if the initialization of SSM parameters is suitable, the slight non-monotonic increase in generalization error under small samples can also be improved.

### B.4 Power Spectrum of Some Datasets

In this section, we present additional figures for Section 4.2. We demonstrate the power spectra of CIFAR-10, Pathfinder, ListOps, and Speech Commands. As shown in Figure B.7, Pathfinder and Speech Commands exhibit substantially richer high-frequency components compared to CIFAR-10. In contrast, ListOps is essentially a symbolic reasoning task and therefore lacks meaningful spectral structure.

### B.5 Training Curves of Deep SSMs

In this part, we demonstrate representative training curves (test loss vs. epoch) for each dataset and training data ratio as supplementary figures for Section 4.2, shown in Figure B.8, Figure B.9,

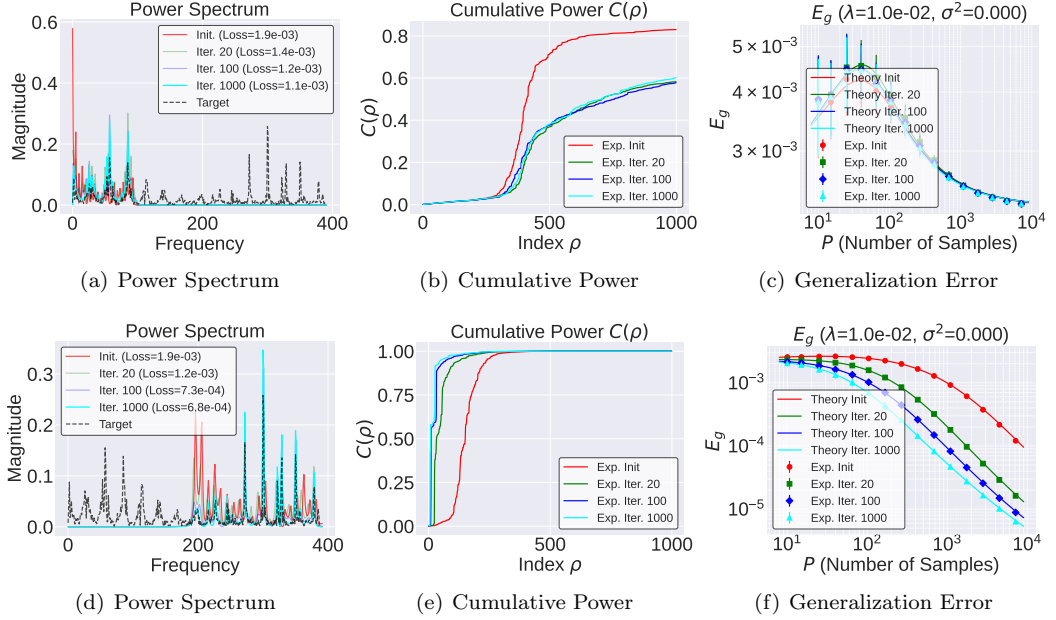


Figure B.6: Comparison on high-frequency task. (a-c): Power spectrum, cumulative power curves and learning curves of low-frequency SSM. (d-f): Power spectrum, cumulative power curves and learning curves of high-frequency SSM. Colored lines denote different optimization iterations, while the black dashed line indicates the target spectrum.

Figure B.10 and Figure B.11. Due to the inherent complexity of deep neural network training, we limit our discussion to high-level observations as follows.

- For tasks with rich frequency components, applying TDI generally leads to lower test loss in the small-data regime (Figures B.9 and B.10).
- When the dataset is sufficiently large (ratio close to 1), the TDI model may be slightly outperformed by the baseline model (Figures B.9 and B.10). This instability in the large-data regime could be due to limiting power spectrum matching to a maximum of 20,000 training samples (see Appendix D.5), or other factors such as suboptimal learning rate, which hinder effective training.
- TDI appears to mitigate overfitting, as evidenced across all four datasets.
- For tasks with poor frequency components, the difference between baseline and TDI remains minimal on small and large data ratios (Figures B.8 and B.11).

## C Supplementary Proofs

This section provides complete proofs of all the theorems and lemmas stated in the main text, with the exception of Theorem 3.4, whose more involved proof is deferred to Appendix E.

### C.1 Characterizing SSM-Induced Kernel

We first present proofs characterizing the SSM-induced kernel. We begin by recalling our definition of SSM-induced kernel in Section 3.1.

**Definition 1** (SSM-Induced Kernel). *Let  $\mathbf{u}, \mathbf{u}' \in \mathbb{R}^L$  be two input sequences of length  $L$ . The SSM-induced kernel is defined as the inner product of their corresponding Toeplitz matrix features:  $K(\mathbf{u}, \mathbf{u}') = \frac{1}{L}(\mathbf{T}_K \mathbf{u})^\top (\mathbf{T}_K \mathbf{u}')$ , where  $\mathbf{T}_K$  denotes the Toeplitz matrix defined by the SSM's impulse response kernel.*

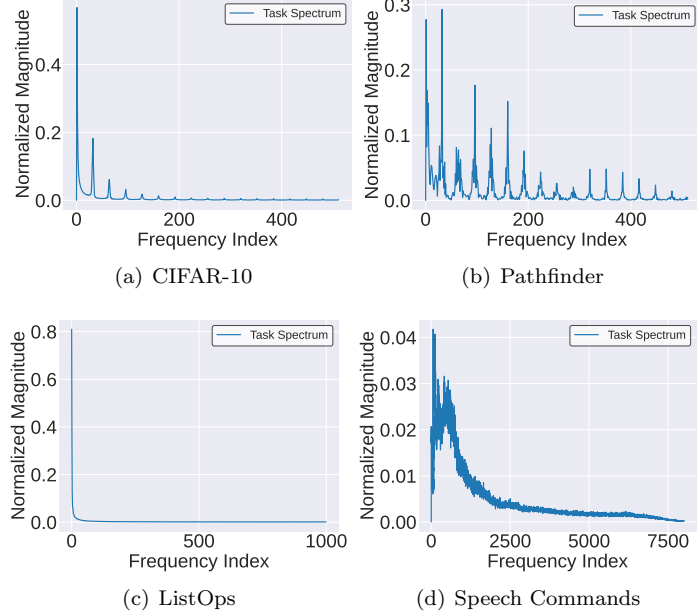


Figure B.7: Power spectrum of real datasets. Pathfinder and Speech Commands exhibit richer high-frequency components than CIFAR-10, and richer spectral content across all frequencies than ListOps.

We first show our kernel is valid by Lemma 3.1.

**Lemma 3.1** (Positive Semi-Definiteness). *The SSM-induced kernel  $K(\mathbf{u}, \mathbf{u}')$  is a valid kernel.*

*Proof of Lemma 3.1.* By definition, for any set of input sequences  $\{\mathbf{u}^1, \dots, \mathbf{u}^P\}$ , the Gram matrix  $\mathbf{K}$  has entries  $\mathbf{K}_{\mu\nu} = K(\mathbf{u}^\mu, \mathbf{u}^\nu) = \frac{1}{L}(\mathbf{T}_K \mathbf{u}^\mu)^\top (\mathbf{T}_K \mathbf{u}^\nu)$ . Let  $\mathbf{U} = [\mathbf{u}^1, \dots, \mathbf{u}^P]$  be the matrix of input sequences. The Gram matrix can be written in matrix form as  $\mathbf{K} = \frac{1}{L}(\mathbf{T}_K \mathbf{U})^\top (\mathbf{T}_K \mathbf{U})$ . For any non-zero vector  $\mathbf{z} \in \mathbb{R}^P$ , we have:

$$\mathbf{z}^\top \mathbf{K} \mathbf{z} = \frac{1}{L} \mathbf{z}^\top (\mathbf{T}_K \mathbf{U})^\top (\mathbf{T}_K \mathbf{U}) \mathbf{z} = \frac{1}{L} \|(\mathbf{T}_K \mathbf{U}) \mathbf{z}\|_2^2 \geq 0.$$

Therefore, since the Gram matrix  $\mathbf{K}$  is positive semi-definite (and symmetric obviously), the kernel  $K(\mathbf{u}, \mathbf{u}')$  is valid.  $\square$

Inserting the singular value decomposition (SVD) of Toeplitz matrix  $\mathbf{T}_K = \sqrt{L} \mathbf{U} \mathbf{S} \mathbf{V}^\top$  into Definition 1, we obtain  $K(\mathbf{u}, \mathbf{u}') = (\mathbf{V}^\top \mathbf{u})^\top \mathbf{S}^2 (\mathbf{V}^\top \mathbf{u}')$ . Then, we prove rows of  $\mathbf{V}^\top \mathbf{u}$  form a set of eigenfunctions of the kernel under Assumption 1.

**Lemma 3.2** (Orthonormal Eigenfunctions). *Under Assumption 1, rows of  $\mathbf{V}^\top \mathbf{u}$  form a set of orthonormal eigenfunctions for the SSM-induced kernel.*

*Proof of Lemma 3.2.* Let  $\mathbf{v}_i^\top$  denote the  $i$ th row of the right singular matrix  $\mathbf{V}^\top$ . For any integer  $i, j \in [1, L]$ ,

$$\int (\mathbf{v}_i^\top \mathbf{u}) \cdot (\mathbf{v}_j^\top \mathbf{u}) p(\mathbf{u}) d\mathbf{u} = \mathbb{E}_{\mathbf{u}} \left[ (\mathbf{V}^\top \mathbf{u} \mathbf{u}^\top \mathbf{V})_{ij} \right] = (\mathbf{V}^\top \mathbb{E}_{\mathbf{u}} [\mathbf{u} \mathbf{u}^\top] \mathbf{V})_{ij} = \delta_{ij}.$$

The last step follows from Assumption 1 and the fact that the columns of  $\mathbf{V}$  are orthonormal vectors.  $\square$

Combining Lemma 3.1, Lemma 3.2 and Mercer's Theorem (Theorem 2.1), we derive Theorem 3.3.

**Theorem 3.3** (Eigen-Decomposition of SSM-Induced Kernel). *Under Assumption 1, given the Toeplitz matrix  $\mathbf{T}_K \in \mathbb{R}^{L \times L}$ , the SSM-induced kernel has a rank at most  $L$ , and its eigen-decomposition is determined by  $K(\mathbf{u}, \mathbf{u}') = \sum_{\rho} \eta_{\rho} \phi_{\rho}(\mathbf{u}) \phi_{\rho}(\mathbf{u}')$ , where  $\eta_{\rho} = s_{\rho}^2$ ,  $\phi_{\rho}(\mathbf{u}) = (\mathbf{V}^\top \mathbf{u})_{\rho}$ , for  $\rho = 1, \dots, L$ .*

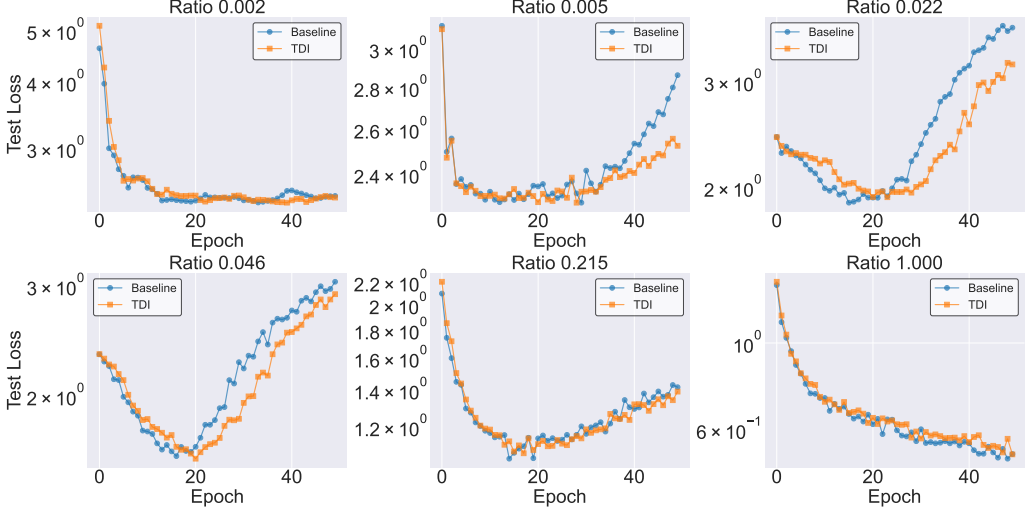


Figure B.8: Training curves on CIFAR-10

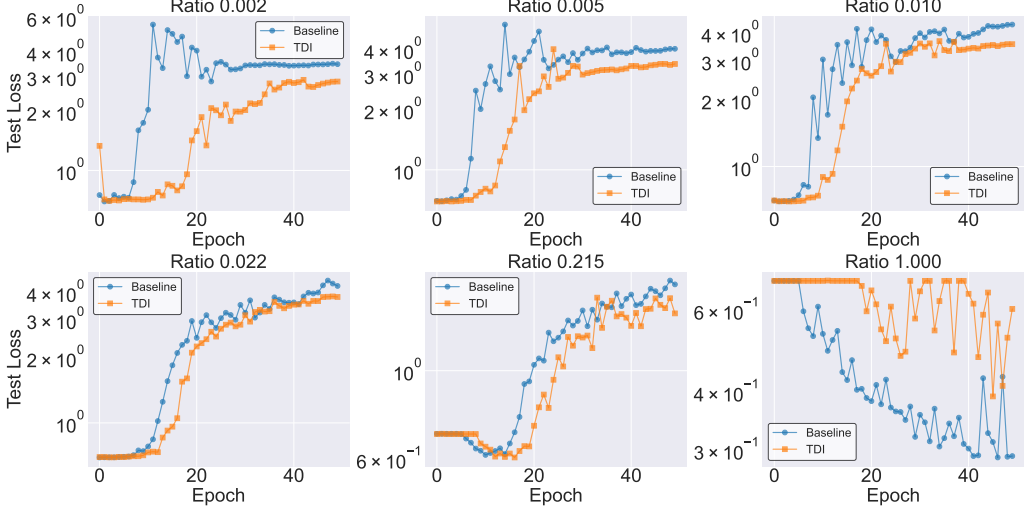


Figure B.9: Training curves on Pathfinder

## C.2 Power Spectrum Matching Improves Generalization

Next, we present proofs showing that minimizing power spectrum matching loss  $\mathcal{L}_{\mathcal{F}}$  improves generalization by promoting a faster rise in cumulative power  $C(\rho)$ .

Let  $|H(\omega)|^2$  denote the model power spectrum derived from the SSM's intrinsic frequency response and  $G_{\mathbf{u}\mathbf{y}}(\omega)$  denote the task power spectrum estimated from the Fourier transform of the input-output cross-variance matrix  $\mathbf{C}_{\mathbf{u}\mathbf{y}} = \mathbb{E}_{\mathbf{u}}[\mathbf{u}\mathbf{y}^\top] \approx \frac{1}{P} \sum_{\mu=1}^P \mathbf{u}^\mu \mathbf{y}^{\mu\top}$ . The power spectrum matching loss is defined in Section 3.4.

**Definition 2** (Power Spectrum Matching Loss). *We define the power spectrum matching loss  $\mathcal{L}_{\mathcal{F}}$  as the squared  $L_2$ -distance between the normalized model and task power spectra:*

$$\mathcal{L}_{\mathcal{F}} = \left\| \frac{|H(\omega)|^2}{\| |H(\omega)|^2 \|_2} - \frac{|G_{\mathbf{u}\mathbf{y}}(\omega)|}{\| |G_{\mathbf{u}\mathbf{y}}(\omega)| \|_2} \right\|_2^2, \quad (4)$$

where  $|G_{\mathbf{u}\mathbf{y}}(\omega)|$  denotes the magnitude of the task's cross-power spectral density, given by  $|\mathcal{F}(\mathbf{C}_{\mathbf{u}\mathbf{y}})|$ , averaged across the label dimension  $d$ .

We provide a two-part theoretical justification. First, we show that maximizing a general alignment objective  $J$ , promotes a rapid increase in  $C(\rho)$  (Lemma 3.5). Then we show that

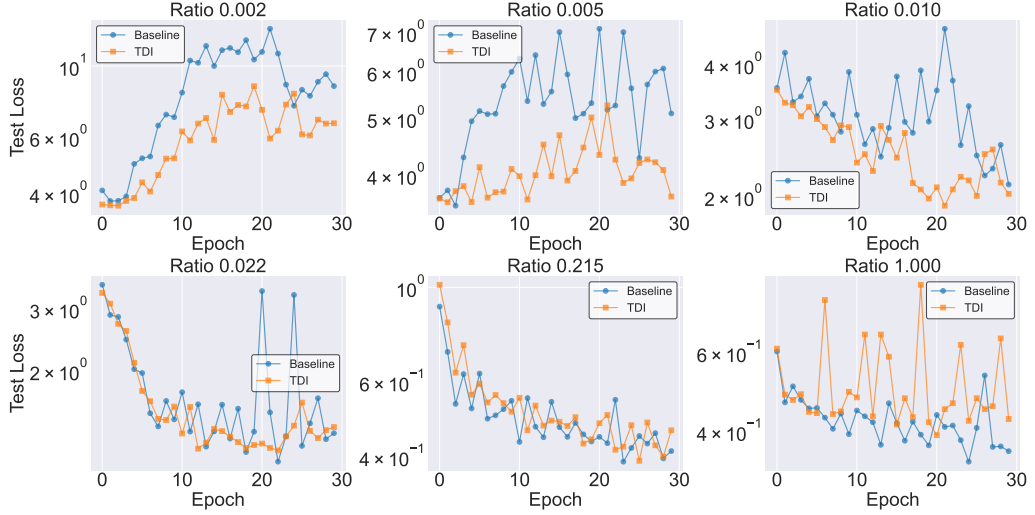


Figure B.10: Training curves on Speech Commands

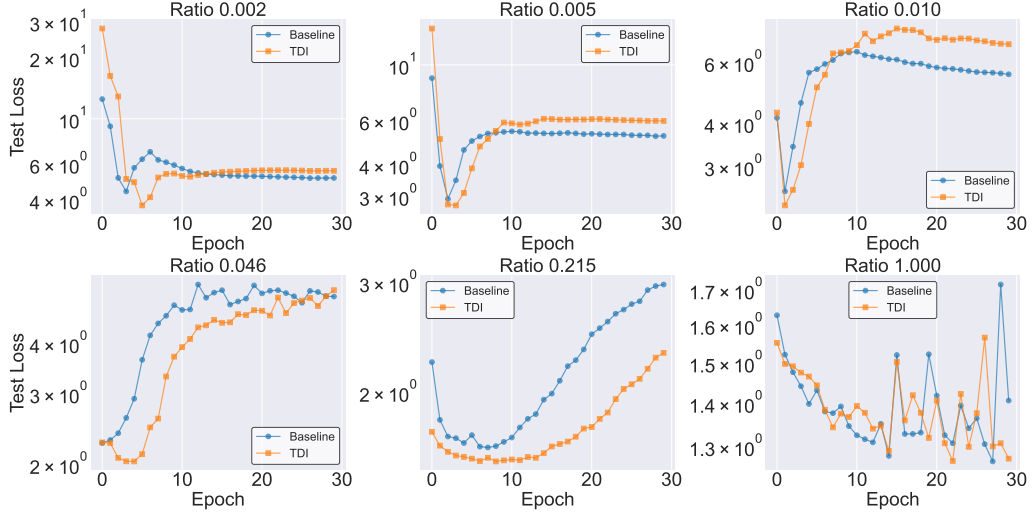


Figure B.11: Training curves on ListOps

minimizing power spectrum matching loss  $\mathcal{L}_F$  is an efficient strategy for maximizing  $J$  (Lemma 3.6).

**Lemma 3.5.** *Maximizing a general alignment objective  $J = K(\mathbf{C}_{\mathbf{u}\mathbf{y}}, \mathbf{C}_{\mathbf{u}\mathbf{y}}) \equiv \frac{1}{L} \|\mathbf{T}_K \mathbf{C}_{\mathbf{u}\mathbf{y}}\|_F^2$  promotes a rapid increase in  $C(\rho)$ , where  $\|\cdot\|_F$  denotes the Frobenius norm.*

*Proof of Lemma 3.5.* Since the eigenfunctions of SSM-induced kernel are linear for any input data  $\mathbf{u}$ , we denote  $\phi_\rho(\mathbf{u}) = \boldsymbol{\alpha}_\rho \mathbf{u}$  where  $\boldsymbol{\alpha}_\rho$  is a linear operator. Let  $\bar{w}_{\rho,j}$  denote the projection coefficient of the  $j$ -th component of  $\mathbf{y}$  onto  $\phi_\rho$ ,

$$\bar{w}_{\rho,j} = \mathbb{E}_{\mathbf{u}}[\phi_\rho(\mathbf{u}) \mathbf{y}_j] = \mathbb{E}_{\mathbf{u}}[\boldsymbol{\alpha}_\rho \mathbf{u} \cdot \mathbf{y}_j] = \boldsymbol{\alpha}_\rho \mathbb{E}_{\mathbf{u}}[\mathbf{u} \cdot \mathbf{y}_j] = \boldsymbol{\alpha}_\rho \mathbf{C}_j = \phi_\rho(\mathbf{C}_j),$$

where  $\mathbf{C}_j$  is the  $j$ -th column of  $\mathbf{C}_{\mathbf{u}\mathbf{y}}$ . Then,

$$J \equiv \frac{1}{L} \|\mathbf{T}_K \mathbf{C}_{\mathbf{u}\mathbf{y}}\|_F^2 = \sum_{\rho=1}^L \eta_\rho \sum_{j=1}^d \phi_\rho(\mathbf{C}_j)^2 = \sum_{\rho=1}^L \sum_{j=1}^d \eta_\rho \bar{w}_{\rho,j}^2 = \sum_{\rho=1}^L \eta_\rho \bar{w}_\rho^2.$$

The last step follows the definition in Section 2. During optimization, both the eigenvalues  $\eta_\rho$  and  $\bar{w}_\rho$  are functions of the SSM parameters being tuned. The eigenvalues are, by definition, sorted in

descending order. By the rearrangement inequality, the sum of products of two sequences is maximized when both sequences are sorted in the same order. To maximize  $J$ , the optimization process is therefore incentivized to find parameters that sort the sequence of  $\{\bar{w}_\rho\}$  in the same descending order as the eigenvalues, which is precisely the condition for a rapidly increasing cumulative power curve. Thus, maximizing  $J$  promotes a faster-rising  $C(\rho)$ .  $\square$

**Lemma 3.6.** *Minimizing power spectrum matching loss  $\mathcal{L}_F$  is equivalent to maximizing  $J$ .*

*Proof of Lemma 3.6.* Expanding the general alignment objective  $J = \frac{1}{L} \|\mathbf{T}_K \mathbf{C}_{\mathbf{u}\mathbf{y}}\|_F^2$  as the sum of squared Euclidean norms,  $J = \frac{1}{L} \sum_{j=1}^d \|\mathbf{T}_K \mathbf{C}_j\|_2^2$  (recall that  $d$  is the dimension of labels). By Parseval’s Theorem, the norm of a vector is proportional to the norm of its Fourier transform. Thus,

$$\|\mathbf{T}_K \mathbf{C}_j\|_2^2 \propto \sum_{\omega} |\mathcal{F}(\mathbf{T}_K \mathbf{C}_j)(\omega)|^2 = \sum_{\omega} \left| \mathcal{F}(\bar{\mathbf{k}} * \mathbf{C}_j) \right|^2 = \sum_{\omega} |H(\omega)|^2 |G_{\mathbf{C}_j}(\omega)|^2,$$

where the last step follows from Convolution Theorem. Substituting this back into the expression for  $J$ , we arrive at the frequency-domain representation,

$$J \propto \sum_{\omega} |H(\omega)|^2 \sum_{j=1}^d |G_{\mathbf{C}_j}(\omega)|^2.$$

This equation shows that  $J$  is proportional to the inner product between the model’s power spectrum and the task’s total power spectrum. By the Cauchy-Schwarz inequality, this inner product is maximized when the two spectra are maximally aligned. Therefore, minimizing  $\mathcal{L}_F$  is an equivalent and efficient method for maximizing the general alignment objective  $J$ .  $\square$

Based on Lemma 3.5 and Lemma 3.6, we derive Theorem 3.7.

**Theorem 3.7** (Power Spectrum Matching Improves Generalization Ability). *Minimizing power spectrum matching loss  $\mathcal{L}_F$  promotes a rapid increase in  $C(\rho)$ , thus improving the generalization ability of SSM-induced kernel by aligning its inductive bias with the task’s frequency spectral properties.*

## D Experimental Details

In this section, we provide some details of our experiments.

### D.1 Diagonalizing Kernel on Real Datasets

Empirical eigenvalues and eigenfunctions are obtained by diagonalizing the Gram matrix of the whole dataset (trainset + testset),  $\mathbf{K}_{\mu\nu} = K(\mathbf{u}^\mu, \mathbf{u}^\nu)$ ,  $\mu, \nu = 1, \dots, M$ , where  $M > P$  denotes the size of the whole dataset. Diagonalizing  $\mathbf{K}$  yields  $\mathbf{K} = M \mathbf{\Phi} \mathbf{\Lambda} \mathbf{\Phi}^\top$ , where the diagonal entries of  $\mathbf{\Lambda}$  are the empirical eigenvalues and the columns of the orthogonal matrix  $\mathbf{\Phi}$  are the empirical eigenvectors. For these empirical eigenfunctions to be orthonormal in the RKHS, they must satisfy the orthonormality condition with respect to the empirical data distribution  $p(\mathbf{u}) = \frac{1}{M} \sum_{\mu=1}^M \delta(\mathbf{u} - \mathbf{u}^\mu)$ . The empirical eigenfunctions are given by  $\sqrt{M} \mathbf{\Phi}$ , because

$$\int (\sqrt{M} \mathbf{\Phi}_{:,i}) \cdot (\sqrt{M} \mathbf{\Phi}_{:,j}) p(\mathbf{u}) d\mathbf{u} = \frac{1}{M} \sum_{\mu=1}^M \sqrt{M} \mathbf{\Phi}_{\mu i} \cdot \sqrt{M} \mathbf{\Phi}_{\mu j} = \delta_{ij}.$$

The last step follows from the fact that  $\mathbf{\Phi}$  is an orthogonal matrix. Thus, the empirical eigenvalues and eigenfunctions derived from the Gram matrix serve as empirical counterparts to the theoretical ones from Theorem 3.3.

Although Theorem 3.3 states that the SSM-induced kernel has a rank of at most  $L$ , the number of non-zero empirical eigenvalues typically exceeds  $L$  due to numerical noise. However, the spectrum of  $\mathbf{K}$  rapidly decays after  $\rho > L$ , and the learned weights in those directions are nearly zero (see Section 3.3). This finding corroborates our theory.

## D.2 Synthetic Task Generation

For the synthetic low- and high-frequency tasks, we generate labels based on MNIST images as follows. Let  $\mathbf{U} \in \mathbb{R}^{P \times L}$  denote the mean-centered MNIST data matrix, with each image reshaped into a vector. We define a temporal grid  $t \in [0, 1]^L$  and construct frequency patterns corresponding to low- or high-frequency components,

$$\begin{aligned} p_{\text{low}}(t) &= \cos(2\pi \cdot 20t) + \cos(2\pi \cdot 40t), \\ p_{\text{high}}(t) &= \cos(2\pi \cdot 300t) + \sin(2\pi \cdot 350t), \end{aligned}$$

which are  $L_2$ -normalized and used to generate labels as  $\mathbf{Y} = \mathbf{U}p$ .

This procedure ensures that the synthetic labels inherit the desired frequency structure while preserving the spatial correlations of MNIST.

## D.3 Optimization of the SSM Parameters

To fit the SSM to a given task, we parameterize it as in Gu et al. [2022b]  $\mathbf{A} = -\exp(\log(-\text{Re } \mathbf{A})) + i \text{Im } \mathbf{A}$ , the output matrix  $\mathbf{C}$ , and time step  $\Delta = \exp(\log dt)$ , where  $\log(-\text{Re } \mathbf{A}), \text{Im } \mathbf{A}, \mathbf{C}, \log dt$  are trainable parameters. For multi-dimensional outputs, we first compute the cross-covariance matrix  $\mathbf{C}_{\mathbf{u}\mathbf{y}} = \mathbf{U}^\top \mathbf{Y}/P$  and the corresponding power spectrum  $G_{\mathbf{u}\mathbf{y}}$ , given by  $|\mathcal{F}(\mathbf{C}_{\mathbf{u}\mathbf{y}})|$  averaged across the label dimension  $d$ .

The SSM parameters are optimized by minimizing the power spectrum matching loss using Adam with a cosine-annealing scheduler. The details are implemented in Algorithm 1.

---

### Algorithm 1 Optimizing S4D Parameter via Power Spectrum Matching

---

```

1: procedure FINDS4D( $G_{\mathbf{u}\mathbf{y}}$ ,  $L$ ,  $N$ ,  $\theta_{\text{init}}$ ,  $\eta$ ,  $T$ )
2:   Input: Task power spectrum  $G_{\mathbf{u}\mathbf{y}}$ , seq length  $L$ , state size  $N$ , initial parameters  $\theta_{\text{init}}$ , learning rate  $\eta$ , iterations  $T$ .
3:   Output: Optimized SSM parameters  $\theta^* = \{\mathbf{A}^*, \mathbf{C}^*, \Delta^*\}$ .
4:   Initialize trainable parameters  $\{\log \mathbf{A}_{\text{real}}, \mathbf{A}_{\text{imag}}, \mathbf{C}, \log \Delta\}$  from  $\theta_{\text{init}}$ .
5:   Initialize Adam optimizer and Cosine Annealing scheduler.
6:   for  $i = 1$  to  $T$  do
7:     Reconstruct  $\mathbf{A}$  and  $\Delta$  from trainable parameters.
8:      $\bar{\mathbf{t}} \leftarrow \text{ComputeS4DImpulseResponse}(\mathbf{A}, \mathbf{C}, \Delta, L)$ 
9:      $\hat{\mathbf{S}}_{\text{ssm}} \leftarrow \text{Normalize}(|\text{FFT}(\bar{\mathbf{t}})|^2)$ 
10:     $\hat{\mathbf{S}}_{\text{task}} \leftarrow \text{Normalize}(|G_{\mathbf{u}\mathbf{y}}|)$ 
11:     $\mathcal{L}_{\mathcal{F}} \leftarrow \text{MSE}(\hat{\mathbf{S}}_{\text{ssm}}, \hat{\mathbf{S}}_{\text{task}})$ 
12:    Update trainable parameters using gradient descent on  $\mathcal{L}_{\mathcal{F}}$ .
13:   end for
14:   Reconstruct final parameters  $\mathbf{A}^*, \mathbf{C}^*, \Delta^*$ .
15:   return  $\{\mathbf{A}^*, \mathbf{C}^*, \Delta^*\}$ 
16: end procedure

```

---

## D.4 Design of Low- and High-Frequency Biased SSMs

In our experiment, the parameters of the low-frequency biased SSM are set by

$$\Delta = \frac{0.5}{N}, \quad \text{Im } \mathbf{A} = \pi \cdot \{0, 1, \dots, \lfloor n/2 \rfloor\},$$

and those of the high-frequency biased SSM are

$$\Delta = \frac{1}{N}, \quad \text{Im } \mathbf{A} = \pi \cdot \{\lfloor n/2 \rfloor, \dots, n-1\},$$

where

$$\mathbf{C} \sim \mathcal{N}(0, \mathbf{I}), \quad \text{Re } \mathbf{A} = \{-0.5, -0.5, \dots, -0.5\}$$

are fixed.

## D.5 Methods and Hyperparameters Used in Deep SSM Training

Both the baseline and TDI models employ the same hyperparameters, with the only distinction being that the first S4 layer of the TDI model is optimized via spectrum matching (see Appendix D.3 and Algorithm 2) by a maximum of 20,000 training samples, i.e.,  $\min(\text{train samples}, 20000)$ . In particular, the imaginary part of  $\mathbf{A}$  in the first layer of the TDI model is initialized by Theorem F.1, where the frequencies  $\omega_k$  correspond to the top 64 values of  $|G_{\mathbf{u}\mathbf{y}}(\omega)|$ , given by  $|\mathcal{F}(\mathbf{C}_{\mathbf{u}\mathbf{y}})|$  averaged across the label dimension  $d$ . All other layers are initialized using S4D-Lin [Gu et al., 2022b]. Each model contains four S4 layers with a state size of 64 and feature dimension of 256. Other hyperparameters are reported in Table 1.

**Algorithm 2** Main Loop for Optimizing the First Layer of Multi-Head Deep SSM Model

---

```

1: Input: Heads  $H$ , initial parameters  $\{\mathbf{A}_{\text{init}}, \mathbf{C}_{\text{init}}, \Delta_{\text{init}}\}$ , task power spectrum  $G_{\mathbf{u}\mathbf{y}}$ .
2: Output: Final multi-head parameters  $\{\mathbf{A}_{\text{final}}, \mathbf{C}_{\text{final}}, \Delta_{\text{final}}\}$ .
3: Initialize empty parameter lists  $\mathcal{A}_{\text{list}}, \mathcal{C}_{\text{list}}, \mathcal{D}_{\text{list}}$ .
4: for  $h = 1$  to  $H$  do
5:   Get initial parameters  $\theta_{\text{init}}^{(h)} = \{\mathbf{A}_{\text{init}}^{(h)}, \mathbf{C}_{\text{init}}^{(h)}, \Delta_{\text{init}}^{(h)}\}$  for head  $h$  by slicing inputs.
6:    $\theta^{*(h)} \leftarrow \text{FINDS4D}(G_{\mathbf{u}\mathbf{y}}, L, N, \theta_{\text{init}}^{(h)}, \dots)$ 
7:   Append learned parameters  $\{\mathbf{A}^{*(h)}, \mathbf{C}^{*(h)}, \Delta^{*(h)}\}$  to lists.
8: end for
9:  $\mathbf{A}_{\text{final}} \leftarrow \text{Concatenate and stabilize}(\mathcal{A}_{\text{list}})$ 
10:  $\mathbf{C}_{\text{final}} \leftarrow \text{Concatenate}(\mathcal{C}_{\text{list}})$ 
11:  $\Delta_{\text{final}} \leftarrow \text{Concatenate}(\mathcal{D}_{\text{list}})$ 
12: if  $\mathbf{C}_{\text{init}}$  has a channel dimension then
13:   Expand  $\mathbf{C}_{\text{final}}$  to match channel dimensions.
14: end if
15: return  $\{\mathbf{A}_{\text{final}}, \mathbf{C}_{\text{final}}, \Delta_{\text{final}}\}$ 

```

---

Table 1: Hyperparameters Used in Deep SSM Training

Dataset	Norm	Pre-norm	Dropout	LR	Batch Size	Epochs	WD
<b>CIFAR-10</b>	Layer	False	0.1	0.01	50	50	0.05
<b>Pathfinder</b>	Batch	True	0.0	0.004	50/70*	50	0.03
<b>ListOps</b>	Batch	False	0.0	0.01	50	30	0.05
<b>Speech Commands</b>	Batch	True	0.0	0.01	20	30	0.05

\* Batch size = 50 for small training sets (ratio  $< 0.2$ ), 70 for larger training sets (ratio  $> 0.2$ ).

## E Relation Between Singular Values of Toeplitz Matrices and the Frequency Response of SSMs

In this section, we analyze the relation between singular values of the SSM's Toeplitz and the frequency response of SSM. We begin by introducing a lemma from Gray et al. [2006].

**Lemma E.1** (Lemma 4.6 of Gray et al. [2006]). *Let  $\mathbf{T}_n(f) = \{t_{k-j}\}_{j,k=0,\dots,n-1}$  where*

$$\sum_{k=-\infty}^{\infty} |t_k| < \infty,$$

*and*

$$f(\lambda) = \sum_{k=-\infty}^{\infty} t_k e^{ik\lambda}, \quad \hat{f}_n(\lambda) = \sum_{k=-(n-1)}^{n-1} t_k e^{ik\lambda}.$$

Define the circulant matrices  $\mathbf{C}_n(f)$  with top row  $(c_0^{(n)}, \dots, c_{n-1}^{(n)})$ , and  $\mathbf{C}_n(\hat{f})$  with top row  $(\hat{c}_0^{(n)}, \dots, \hat{c}_{n-1}^{(n)})$  where

$$c_k^{(n)} = \frac{1}{n} \sum_{j=0}^{n-1} f(2\pi j/n) e^{2\pi i j k / n}, \quad \hat{c}_k^{(n)} = \frac{1}{n} \sum_{j=0}^{n-1} \hat{f}_n(2\pi j/n) e^{2\pi i j k / n}.$$

Then  $\mathbf{C}_n(f) \sim \mathbf{C}_n(\hat{f}_n) \sim \mathbf{T}_n$  as  $n \rightarrow \infty$ .

Lemma E.1 states that as  $n \rightarrow \infty$ ,  $\mathbf{T}_n$  is asymptotically equivalent to a circulant matrix  $\mathbf{C}_n(f)$  or  $\mathbf{C}_n(\hat{f})$ . Based on the fact that the eigenvalues of a circulant matrix are given by the discrete Fourier transform of its top row  $(c_0^{(n)}, \dots, c_{n-1}^{(n)})$ ,

$$\lambda_k = \sum_{j=0}^{n-1} c_j^{(n)} e^{-2\pi i j k / n},$$

we obtain

$$\lambda_k(\mathbf{C}_n(f)) = \sum_{j=0}^{n-1} \frac{1}{n} \sum_{l=0}^{n-1} f(2\pi l/n) e^{2\pi i j l / n} e^{-2\pi i j k / n} = f(2\pi k/n) = \sum_{p=-\infty}^{\infty} t_p e^{ip \cdot 2\pi k / n}.$$

Since  $\mathbf{C}_n$  is circulant, its singular values  $s_k$  are equal to the absolute value of its eigenvalues  $\lambda_k$ . Thus we arrive at

$$s_k(\mathbf{T}_n) \sim s_k(\mathbf{C}_n) = |\lambda_k(\mathbf{C}_n)| = \left| \sum_{p=-\infty}^{\infty} t_p e^{ip \cdot 2\pi k / n} \right|.$$

For the SSM's Toeplitz matrix,  $t_p = \bar{\mathbf{t}}_{-p}$  (see Section 2.2). Then,  $t_{p>0} = 0, t_{p\leq 0} = \bar{\mathbf{t}}_{-p}$  is the impulse response kernel of SSM. Then,

$$s_k = \left| \sum_{p=-\infty}^{\infty} t_p e^{ip \cdot 2\pi k / n} \right| = \left| \sum_{p=0}^{\infty} \bar{\mathbf{t}}_p e^{-ip\omega_k} \right| = |H(\omega_k)|,$$

where  $\omega_k = \frac{2\pi k}{n}$  ( $k = 0, \dots, n-1$ ) and  $H(\omega)$  is exactly the frequency response (or transfer function) of the SSM (see Section 2.2). We summarize this result in Theorem E.2.

**Theorem E.2** (Asymptotic Behavior of Singular Values). *For large  $n$ , the  $k$ -th singular value  $s_k$  of the SSM's Toeplitz matrix  $\mathbf{T}_K \in \mathbb{R}^{n \times n}$  is equal to the frequency response  $|H(\omega_k)|$ , where  $\omega_k = \frac{2\pi k}{n}$  for  $k = 0, \dots, n-1$ .*

Similar to the derivation of singular values, we can analogously show that the  $k$ -th row of  $\mathbf{V}^\top$  corresponds to the Fourier basis with frequency  $\omega_k$ .

**Theorem E.3** (Asymptotic Behavior of Right Singular Vectors). *For large  $n$ , the  $k$ -th row of the right singular matrix  $\mathbf{V}^\top$  of the SSM's Toeplitz matrix  $\mathbf{T}_K \in \mathbb{R}^{n \times n}$  is equal to the Fourier basis with frequency  $\omega_k$  for  $k = 0, \dots, n-1$ .*

It is worth noting that the singular values and the right singular matrix are not sorted here; the index  $k$  refers to the corresponding frequency  $\omega_k = \frac{2\pi k}{n}$ .

In the unwhitened data case,  $\tilde{\mathbf{T}}$  defined in Section 3.2 can be expressed as  $\tilde{\mathbf{T}} = \mathbf{U} \mathbf{S} \mathbf{V}^\top \mathbf{Q} \mathbf{D} \mathbf{Q}^\top$ , where  $\mathbf{Q} \mathbf{D} \mathbf{Q}^\top = \Sigma^{\frac{1}{2}}$ . Thus, the SVD of  $\tilde{\mathbf{T}}$  is determined by the SVD of  $\mathbf{M} = \mathbf{S}(\mathbf{V}^\top \mathbf{Q}) \mathbf{D}$ , where  $\tilde{\mathbf{T}} = \mathbf{U} \mathbf{U}_M \Sigma_M \mathbf{V}_M^\top \mathbf{Q}^\top$  for  $\mathbf{M} = \mathbf{U}_M \Sigma_M \mathbf{V}_M^\top$ . Since both  $\mathbf{V}^\top$  and  $\mathbf{Q}$  are orthogonal,  $\mathbf{V}^\top \mathbf{Q}$  is itself an orthogonal change of basis: it maps the Fourier basis  $\mathbf{V}^\top$  into the eigenbasis of the data covariance (columns of  $\mathbf{Q}$ ). Therefore, the singular values of  $\mathbf{M}$ , and hence of  $\tilde{\mathbf{T}}$ , are governed by how the frequency response encoded in  $\mathbf{S}$  aligns with the spectral distribution of the high-variance directions encoded in  $\mathbf{D}$ . In particular, a large singular value arises when a dominant data mode (large  $\mathbf{D}_j$ ) has most of its energy concentrated in frequencies where the LTI operator exhibits strong gain, resulting in faster learning at the corresponding basis. Actually, our power spectrum matching method in Section 3.4 is inspired by this finding.

## F Further Analysis of SSM's Frequency Bias

In this section, we will analyze the relation between frequency bias of an SSM and its parameters.

First, we restate the definition of frequency bias in Yu et al. [2024]: frequency bias of an SSM means that the frequency responses of the systems have more variation in the low-frequency area than the high-frequency area.

The frequency response  $H(\omega)$  of an SSM is actually the discrete Fourier transform of its impulse response  $\bar{\mathbf{t}}$ ,

$$H(\omega) = \text{DFT}(\bar{\mathbf{t}}) = \sum_{n=0}^{\infty} \bar{\mathbf{t}}_n e^{-i\omega n}, \quad \omega \in (0, 2\pi).$$

Substituting  $\bar{\mathbf{t}}_n = \bar{\mathbf{C}} \bar{\mathbf{A}}^n \bar{\mathbf{B}}$ ,

$$H(\omega) = \sum_{n=0}^{\infty} \bar{\mathbf{C}} \bar{\mathbf{A}}^n \bar{\mathbf{B}} e^{-i\omega n} = \bar{\mathbf{C}} (\bar{\mathbf{I}} - \bar{\mathbf{A}} e^{-i\omega})^{-1} \bar{\mathbf{B}}.$$

We substitute  $\mathbf{A}, \mathbf{B}, \mathbf{C}, \Delta$  into  $\bar{\mathbf{A}}, \bar{\mathbf{B}}, \bar{\mathbf{C}}$ , and set  $\mathbf{B} = \mathbf{1} \in \mathbb{R}^{n \times 1}$  (fixed  $\mathbf{B}$  in S4D training), we derive

$$H(\omega) = \sum_k \mathbf{C}_k (e^{\Delta \mathbf{A}_k} - 1) \frac{1}{\mathbf{A}_k} \frac{1}{1 - e^{-i\omega + \Delta \mathbf{A}_k}},$$

where  $\mathbf{A}_k$  denotes the  $k$ -th diagonal element of  $\mathbf{A}$  and  $\mathbf{C}_k$  denotes the  $k$ -th element of  $\mathbf{C}$ . This result is similar to equation (3) in Yu et al. [2024].  $|H(\omega)|$  attains an extremum when the denominator reaches its extremum, which is given by

$$\frac{d}{d\omega} \text{Re} e^{-i\omega + \Delta(\text{Re} \mathbf{A}_k + i \text{Im} \mathbf{A}_k)} = 0.$$

Thus,  $\omega = \Delta \text{Im} \mathbf{A}_k$  gives the location of the extremum of  $|H(\omega)|$ . Additionally, the corresponding  $\mathbf{C}_k$  and  $\text{Re} \mathbf{A}_k$  determine the magnitude at  $\omega_k = \Delta \text{Im} \mathbf{A}_k$ .

**Theorem F.1.** *Let  $|H(\omega)|$  be the frequency response of an S4D-like SSM with parameters  $\mathbf{A} \in \mathbb{C}^{n \times n}, \mathbf{C} \in \mathbb{C}^{1 \times n}, \Delta \in \mathbb{R}$ . Then, the location of its extremum is determined by  $\omega_k = \Delta \text{Im} \mathbf{A}_k$ , whereas the magnitude of the extremum is determined by  $\text{Re} \mathbf{A}$  and  $\mathbf{C}$ .*

This result can successfully explain the frequency bias of the SSM. We now provide an estimate for S4D. Since the original S4D initialization gives

$$\mathbf{A}_k = -0.5 + i\pi \cdot k, \quad k = 1, \dots, \lfloor n/2 \rfloor,$$

the extremum points are then determined by  $\omega_k = \pi \Delta k$ . Typically, the number of states,  $n$ , is 64, and  $\Delta$  is sampled from a log-uniform distribution between 0.001 and 0.1. Thus, the proportion of the largest  $\omega_k$  relative to  $\pi$ ,  $\omega_n/\pi = \Delta \cdot \lfloor n/2 \rfloor$  satisfies a log-uniform distribution between 0.032 and 3.2. Thus,  $P(\omega_n/\pi < 0.1) = 0.25, P(\omega_n/\pi < 0.3) = 0.49, P(\omega_n/\pi < 0.6) = 0.64$ . This result shows that with the initialization of S4D, the informative frequency response, i.e., frequency area with more variation, has a high probability to concentrate in a narrow, low-frequency area, causing a low frequency bias of SSM. The first approach to tuning the frequency bias in Yu et al. [2024], involving the simultaneous multiplication of all frequencies by a coefficient, is equivalent to adjusting the range of  $\Delta$ .

Theorem F.1 also provides an instruction on SSM parameter initialization. With inappropriate initialization, double descent of minimizing the power spectrum matching loss  $\mathcal{L}_F$  may lead to local minima (see Appendix B.3). Thus, it is crucial to design an initialization that guides the optimizer toward the correct solution. For example, the imaginary part of  $\mathbf{A}_k$  can be initialized according to Theorem F.1, as detailed in Appendix D.5.